Dysfunctional mechanotransduction regulates the progression of PIK3CA-driven vascular malformations

Wen Yih Aw[1], Aanya Sawhney[1], Mitesh Rathod[1], Chloe P. Whitworth[1,2], Elizabeth L. Doherty[1], Ethan Madden[2], Jingming Lu[1], Kaden Westphal[1], Ryan Stack[1], and William J. Polacheck[1,3,4,*]

[1]Joint Department of Biomedical Engineering, University of North Carolina at Chapel Hill and North Carolina State University, Chapel Hill, NC and Raleigh, NC, USA

[2]Department of Genetics and Molecular Biology, University of North Carolina at Chapel Hill School of Medicine, Chapel Hill, NC, USA

[3]Department of Cell Biology and Physiology, University of North Carolina at Chapel Hill School of Medicine, Chapel Hill, NC, USA

[4]McAllister Heart Institute, University of North Carolina at Chapel Hill School of Medicine, Chapel Hill, NC, USA

*Correspondence: polacheck@unc.edu

Abstract

Somatic activating mutations in *PIK3CA* are common drivers of vascular and lymphatic malformations. Despite common biophysical signatures of tissues susceptible to lesion formation, including compliant extracellular matrix and low rates of perfusion, lesions vary in clinical presentation from localized cystic dilatation to diffuse and infiltrative vascular dysplasia. The mechanisms driving the differences in disease severity and variability in clinical presentation and the role of the biophysical microenvironment in potentiating progression are poorly understood. Here, we investigate the role of hemodynamic forces and the biophysical microenvironment in the pathophysiology of vascular malformations, and we identify hemodynamic shear stress and defective endothelial cell mechanotransduction as key regulators of lesion progression. We found that constitutive PI3K activation impaired flow-mediated endothelial cell alignment and barrier function. We show that defective shear stress sensing in *PIK3CA*^{E542K} endothelial cells is associated with reduced myosin light chain phosphorylation, junctional instability, and defective recruitment of vinculin to cell-cell junctions. Using 3D microfluidic models of the vasculature, we demonstrate that *PIK3CA*^{E542K} microvessels apply reduced traction forces and are unaffected by flow interruption. We further found that draining transmural flow resulted in increased sprouting and invasion responses in *PIK3CA*^{E542K} microvessels. Mechanistically, constitutive PI3K activation decreased cellular and nuclear elasticity resulting in defective cellular tensional homeostasis in endothelial cells which may underlie vascular dilation, tissue hyperplasia, and hypersprouting in *PIK3CA*-driven venous and lymphatic malformations. Together, these results suggest that defective nuclear mechanics, impaired cellular mechanotransduction, and maladaptive hemodynamic responses contribute to the development and progression of *PIK3CA*-driven vascular malformations.

Key words

Vascular malformations, PIK3CA, hemodynamics, mechanotransduction, transmural flow, vascular tissue engineering, organs-on-chip

Introduction

Vascular malformations (VMs) are a class of rare genetic disorders associated with localized developmental abnormalities of venous, arterial, capillary, or lymphatic vessels [1-4]. Histologically, VMs are characterized by complexes of structural lesions with enlarged, irregular lumens that are lined with vascular endothelial cells (ECs) and surrounded by disorganized extracellular matrix [3, 5]. These lesions are often congenital, progress in severity over time, are associated with vascular obstruction and impaired drainage, and can be life threatening. Treatment for VMs, especially for complex malformations that occur in multiple tissues, is difficult and rarely curative, and the standard of care relies on surgery, sclerotherapy, and a limited repertoire of drugs.

VMs are caused by somatic mutations in genes that are involved in vascular development, and these same genes are commonly implicated in malignant tumor angiogenesis [4]. VMs are classified based on blood flow dynamics and are categorized as either slow-flow or fast-flow malformations [3]. The majority of slow-flow malformations, which do not involve an arterial component, are caused by mutations that result in upregulated phosphoinositide 3-kinase (PI3K) and mammalian target of rapamycin (mTOR) signaling [4]. In particular, somatic activating mutations of *PIK3CA* have been identified as the cause of the majority (~80%) of cystic lymphatic malformations, and other pathologies, including generalized lymphatic anomalies, capillary malformations, and venous malformations [2, 6-9]. Several studies have demonstrated that overstimulation of PI3K signaling, independent of genetic mutations in *PIK3CA,* is associated with the pathological development of slow-flow VMs, including cerebral cavernous malformation [10-13] and fast-flow arteriovenous malformations in mouse models of hereditary hemorrhagic telangiectasia [14-16]. Given the implication of PI3K overactivation in both slow- and fast-flow VMs, understanding how hemodynamic forces contribute to the pathogenesis of *PIK3CA*-driven VMs could shed light on novel therapeutic approaches for various vascular anomalies.

PIK3CA encodes the p110α catalytic subunit (PI3Kα) of phosphatidylinositol-3-kinases (PI3K), a lipid kinase that is ubiquitously expressed and essential for regulating effector signaling pathways involved in cell proliferation, metabolism, migration, and survival [17]. At the cellular level, PI3K is activated by receptor tyrosine kinases, focal adhesion kinase, and G-protein coupled receptor signaling [17]. Upon activation, PI3K catalyzes the production of phosphatidylinositol 3,4,5-bisphosphate (PtdIns(3,4,5)P_3 or PIP3) at the plasma membrane, leading to membrane translocation and downstream activation of AKT and mTOR signaling cascades that promote cell growth and survival [17]. PI3K signaling is also involved in the remodeling of the actin cytoskeleton. In particular, activation of PI3Kα has been demonstrated to modulate actomyosin contractility and cell motility in endothelial cells by regulating the activity of myosin light chain phosphatase [18], Rac1- [19], and RhoA-GTPases [20]. In addition to being regulated by growth factors signaling, PI3K functions downstream of the fluid shear stress sensitive mechanosensory complex that consists of platelet endothelial cell adhesion molecule 1 (PECAM-1), vascular endothelial (VE-) cadherin, and vascular endothelial growth factor receptor 2 (VEGFR2) [21-23]. While shear-stress induced activation of PI3K signaling is associated with endothelial cell elongation, alignment, and vasodilatory response, how overactivation of PI3K signaling impacts endothelial mechanotransduction remains unknown.

Multiple studies using mouse models have revealed that PI3Kα plays a crucial role in regulating venous and lymphatic vessel growth and development [6-9, 24-26]. Both the loss of function and inhibition of PI3Kα result in embryonic lethality due to deficient angiogenesis and venous fate

specification [24, 27]. Conversely, expression of gain-of-function *PIK3CA*^{H1047R} variant of PI3Kα in the endothelium leads to over-proliferation of venous and lymphatic endothelial cells [25, 26]. Interestingly, expression of the same oncogenic *PIK3CA*^{H1047R} variant resulted in distinct vascular overgrowth and malformation defects in blood and lymphatic vessels [25]. Specifically, *PIK3CA*-driven vascular malformations manifest as locally restricted vessel overgrowth and dilation in veins and capillaries, but as dense hypersprouting vascular networks in the lymphatics [25]. However, the mechanisms by which one *PIK3CA* activating mutation produces distinct pathological phenotypes in different vascular beds remain to be investigated. The lack of arterial involvement in slow-flow VMs, together with common biophysical signatures of tissues susceptible to lesion formation including compliant extracellular matrix, low rates of perfusion, and drainage flow, suggest significant contributions of vascular hemodynamics and the biophysical microenvironment to *PIK3CA*-driven lesion progression.

Previously, we established a microphysiological model of VMs and identified that *PIK3CA* activating mutations result in elevated Rac1 activity in endothelial cells, which drives lesion formation through dysregulated cytoskeletal dynamics [19]. In this study, we address the role of fluid shear stress and the biophysical microenvironment in the development of *PIK3CA*-driven slow-flow malformations, and we identify hemodynamic shear stress and defective cellular mechanotransduction as key regulators of malformation progression. We demonstrate that endothelial cells expressing *PIK3CA*^{E542K} activating mutation fail to elongate, align, and establish diffusive barrier function in response to laminar shear stress. We observe increased cellular and nuclear compliance, and we further identified deficient recruitment of vinculin, a mechanosensitive adaptor protein, to intercellular adherens junctions in human umbilical vein endothelial cells (HUVECs) expressing a PIK3CA activating mutation commonly associated with VMs. Additionally, using tissue-engineered microvessels, we demonstrate that mutant HUVECs form dilated microvessels that are insensitive to flow interruption and are hypersensitive to basal-to-apical transmural drainage, resulting in sprouting and invasion responses to transmural flow. These results demonstrate that altered endothelial cellular and nuclear mechanical properties, as well as dysfunctional mechanotransduction of hemodynamic stresses, contribute to pathological vascular overgrowth and hypersprouting in *PIK3CA*-driven VMs.

Results

Constitutive PI3K activation impedes flow-mediated ECs remodeling and alignment to laminar shear stress.

The development of PIK3CA-driven vascular lesions is restricted to slow-flow regions of the vasculature [28]. To determine whether VM causal mutations in *PIK3CA* impact mechanotransduction of hemodynamic shear stress, we generated human umbilical vein endothelial cells (HUVECs) expressing wild-type *PIK3CA* (*PIK3CA*^{WT}) or *PIK3CA* harboring a *PI3K*-activating mutation (*PIK3CA*^{E542K}), as described previously [19], and applied flow via orbital shaking (**Figure 1**). This approach allowed us to apply a range of shear stresses, both laminar and oscillatory, to cultured *PIK3CA*^{WT} and *PIK3CA*^{E542K} monolayers. At a wall shear stress magnitude similar to that experienced by venous ECs (~11 dyn/cm^2) [29, 30] near the edge of the well, *PIK3CA*^{WT} HUVECs became highly elongated and aligned with the local flow direction (**Figure 1A-C**). In response to lower magnitude wall shear stress and oscillatory flow toward the center of the well, *PIK3CA*^{WT} HUVECs adopted a more isometric morphology (**Figure 1A, C**). In contrast, *PIK3CA*^{E542K} HUVECs remained isometric at all magnitudes of wall shear stress (**Figure 1A-C**). We further observed increased cell density in *PIK3CA*^{E542K} HUVECs across all applied

shear stress magnitudes, indicating impaired flow-mediated quiescence with excess PI3K activation (**Figure 1D**). Consistent with orbital shaking results, *PIK3CA*^{E542K} HUVECs remained misaligned and overcrowded in response to 10 dyn/cm^2 laminar shear stress applied in a Hele-Shaw flow cell (**Figure 1F**).

To determine if the defective mechanotransduction we observed in blood endothelial cells could play a role in lymphatic malformation progression, we generated lymphatic endothelial cells (LECs) expressing either *PIK3CA*^{WT} or *PIK3CA*^{E542K} (**Figure S1**). Similar to *PIK3CA*^{E542K} HUVECs, we observed that *PIK3CA*^{E542K} LECs were larger in cell size and more isometric compared to *PIK3CA*^{WT} LECs in response to orbital shaking (**Figure S1**), suggesting that excess PI3K activation and effector signaling perturb mechanotransduction of hemodynamic shear stress in both the blood and the lymphatic endothelium. To determine the functional consequences of cellular misalignment to flow, we measured the permeability of *PIK3CA*^{WT} and *PIK3CA*^{E542K} HUVEC monolayers in response to flow. We cultured *PIK3CA*^{WT} and *PIK3CA*^{E542K} HUVEC under orbital shaking conditions on biotinylated-fibronectin substrates, and permeability was quantified by fluorescence intensity of Cy3-conjugated streptavidin that bound to the biotinylated surface (**Figure 1A, E**). In agreement with previous reports [31], we observed improved barrier function in *PIK3CA*^{WT} HUVECs at regions corresponding to high laminar shear stress and a gradual increase in permeability with decreasing wall shear stress magnitude (**Figure 1A, E**). Interestingly, *PIK3CA*^{E542K} HUVECs demonstrated a dichotomous relationship between shear stress magnitude and barrier function, with increased permeability as compared to wild-type cells at high magnitudes of shear stress and reduced permeability at lower shear stress magnitudes (**Figure 1A, E**). Collectively, these findings demonstrated that constitutive PI3K activation hinders flow-mediated endothelial cell alignment and barrier function.

Priming with hemodynamic shear stress prior to PIK3CA^{E542K} *induction restores cell alignment but does not impact permeability.*

To establish the temporal relationship between elevated PI3K signaling, defective endothelial cell remodeling, and loss of vascular barrier function, we generated HUVECs expressing either *tet-ON-PIK3CA*^{WT} or *tet-ON-PIK3CA*^{E542K} in which the expression of WT or mutant variant of *PIK3CA* can be induced by the addition of doxycycline (**Figure S2A**). Treatment with doxycycline to induce *PIK3CA*^{WT} *or PIK3CA*^{E542K} expression induced similar levels of p110α expression as measured by Western blot, indicating a comparable level of lentivirus integration and protein overexpression in both cell lines (**Figure S2A**). Upon addition of doxycycline, we observed increased levels of phospo-AKT1(Ser473) in *tet-ON-PIK3CA*^{E542K}, but not in *tet-ON-PIK3CA*^{WT} endothelial cells, demonstrating activation of PI3K effector signaling in response to induction (**Figure S2A**). To verify the functional relevance of this construct, we generated 3D human microvascular networks with *tet-ON-PIK3CA*^{E542K} HUVECs (**Figure S2B-C**). We observed that the addition of doxycycline during seeding of *tet-ON-PIK3CA*^{E542K} HUVECs accelerated lumenogenesis and resulted in the formation of microvascular networks with enlarged and irregular lumens (**Figure S2B**), in agreement with our previous study demonstrating that constitutive activation of PIK3CA^{E542K} resulted in pathologic network formation [19].

To establish the temporal relationships between dysregulated PI3K activation and mechanotransduction of hemodynamic shear stress, we induced expression of *PIK3CA*^{E542K} either prior to or after the application of flow (**Figure 2A**). When *PIK3CA*^{E542K} expression was induced before the application of flow, ECs remained unresponsive to shear stress, as measured by cell orientation and elongation (**Figure 2A-C**). However, when *PIK3CA*^{E542K} expression was

176 triggered one day after flow, flow-conditioned HUVECs remained elongated and aligned parallel
177 to the flow direction (**Figure 2A-C**). Interestingly, although flow preconditioning rescued cell
178 morphology and alignment, PI3K activation significantly reduced vascular barrier function
179 compared with uninduced (no doxycycline) control (**Figure 2D**). Collectively, these results indicate
180 a mechanistic separation between flow-mediated cell alignment and barrier function, whereby
181 excessive PI3K signaling may have a more direct and immediate impact on EC adherens junction
182 stability and resultant permeability.

183 *Mutant ECs are characterized by adherens junction instability*

184 We previously reported the presence of discontinuous VE-cadherin-containing adherens
185 junctions, decreased cortical actin localization, and increased stress fibers formation in HUVECs
186 expressing *PIK3CA* activating mutations [19]. We observed similar decreased in the distribution
187 of cortical actin, lack of stress fibers alignment, and reduced VE-cadherin signal in cell-cell
188 contacts of flow-conditioned *PIK3CA*^{E542K} HUVECs (**Figure 3A-D**). Additionally, we observed
189 increased microtubule density and similar loss of microtubule and vimentin alignment in
190 *PIK3CA*^{E542K} HUVECs (**Figure S3 and S4**). These findings suggest that the mechanical coupling
191 between the cytoskeleton and adhesion complexes and stability of VE-cadherin adhesion
192 complexes may be hampered with constitutive PI3K activation. To quantify the stability of VE-
193 cadherin intercellular adherens junctions, a VE-cadherin pulse-chase experiment was performed
194 (**Figure 4A-C**). Surface-pool of VE-cadherin were pulse-labeled with non-functional blocking
195 antibody and turnover of labeled VE-cadherin complexes were quantified after a 2-hour chase
196 period. We observed a reduced level of labeled VE-cadherin at cell-cell contacts and a significant
197 increase in the number of internalized labeled VE-cadherin positive vesicles within the cytoplasm
198 of *PIK3CA*^{E542K} HUVECs (**Figure 4A-C**), indicating that adherens junctions are indeed less stable
199 in mutant endothelium. Given that endothelial mechanotransduction of shear stress is partially
200 mediated by cortical Src kinase activation driven by the formation of junctional VE-
201 cadherin/PECAM-1/VEGFR2 mechanosensory complex [23], we investigated the dynamics of
202 Src kinase activation in *PIK3CA* mutant endothelium (**Figure 4D-E**). Interestingly, we found that
203 the temporal dynamics of Src activation measured by the level of phospho-Src (Tyr416) was
204 similar both in magnitude and temporal activation among untransduced HUVEC, PIK3CA^{WT}, and
205 PIK3CA^{E542K} HUVECs (**Figure 4D-E**), suggesting that while assembly and turnover of adherens
206 junctions are disrupted in mutant endothelial cells, some elements of downstream effector
207 signaling remain functional.

208 *Defective recruitment of vinculin at adherens junctions in PIK3CA mutant endothelium.*

209 VE-cadherin containing junctions are mechanically connected to the actin cytoskeleton through
210 the interaction of VE-cadherin with β- and α-catenin [32, 33]. Under mechanical load, tensile
211 stress unfolds α-catenin, allowing for vinculin binding to α-catenin and subsequent force-
212 dependent strengthening of cell-cell junctions [34-36]. To address whether the mechanical
213 coupling between actin cytoskeleton and adhesion complexes could underlie the increased
214 permeability in mutant endothelium, we investigated the spatial localization of vinculin in
215 *PIK3CA*^{WT} and *PIK3CA*^{E542K} HUVECs (**Figure 5A-C**). In *PIK3CA*^{WT} HUVECs, vinculin localized at
216 the cell cortex and co-localized with VE-cadherin containing cell-cell adhesions and along actin
217 stress fibers (**Figure 5A-B**). In contrast, *PIK3CA*^{E542K} HUVECs demonstrated reduced recruitment
218 of vinculin to intercellular adherens junctions as compared to *PIK3CA*^{WT} HUVECs (**Figure 5A-B**).
219 We further observed that while vinculin primarily localizes in a straight and linear pattern in focal
220 adhesion plaques of *PIK3CA*^{WT} HUVECs, vinculin appears as larger, dot-like structures in flow-

221 conditioned *PIK3CA*^{E542K} HUVECs (**Figure 5C**). Despite significant changes in vinculin
222 localization, western blot analysis showed no measurable differences in the amounts of VE-
223 cadherin, β-catenin, and vinculin between control and mutant HUVECs (**Figure 5D-E**).
224 Interestingly, in probing for changes for overall actomyosin contractility, we observed reduced
225 level of phosphorylated myosin light chain II (pMLC2) in mutant ECs compared with control ECs
226 (**Figure 5D-E**). These data demonstrate defective transmission of mechanical forces and
227 stabilization of cell-cell and cell-matrix adhesion complexes in *PIK3CA*^{E542K} HUVECs.

228 *PIK3CA*^{E542K} *HUVECs form dilated microvessels with increased sprouting and reduced traction*
229 *forces.*

230 To relate our findings in 2D cell culture to the pathophysiological phenotype of vascular
231 malformations, we generated and characterized the effect of flow on *PIK3CA*^{WT} or *PIK3CA*^{E542K}
232 tissue engineered human microvessels (**Figure 6**). Engineered microvessels were molded using
233 an acupuncture needle to generate a hollow 160-μm cylindrical channel lined with HUVECs and
234 fully embedded within 2.5 mg/mL type I collagen hydrogel [31, 37]. Cyclic flow of approximately
235 1-3 dyn/cm^2 was imparted by culturing microvessels on a laboratory rocker [37]. After two days of
236 culture under a slow flow environment, *PIK3CA*^{WT} HUVECs formed uniform microvessels with a
237 limited number of sprouts and no apparent HUVEC invasion into the subluminal matrix (**Figure**
238 **6A-B**). In contrast, *PIK3CA*^{E542K} microvessels were significantly dilated and developed numerous
239 sprouts along the vessel length (**Figure 6A-B**). The expanded mutant vessel diameter coincides
240 with an increased number of *PIK3CA*^{E542K} HUVECs, implicating defective regulation of flow-
241 mediated quiescence with excessive PI3K signaling. Treatment with rapamycin, an mTOR
242 inhibitor, or alpelisib, a PIK3CA-specific kinase inhibitor, reduced vessel dilation (**Figure 6A-B**).
243 Importantly, when compared to rapamycin, we observed a more effective reduction in number of
244 sprouts with alpelisib treatment (**Figure 6A-B**). This observation is consistent with our previous
245 finding and the notion that in addition to contributing to uncontrolled growth through downstream
246 mTORC1/2 and growth signaling activation, PI3K hyperactivation alters cytoskeletal dynamics
247 and mechanical properties of endothelial cells [19].

248 Given the defective recruitment of vinculin to adherens junctions, increased vascular permeability,
249 loss of cortical actin organization, and prominent stress fiber formation in *PIK3CA*^{E542K} HUVECs,
250 we reasoned that the dilated microvessel phenotype may reflect reduced cell-cell adhesion
251 strength and altered cell-matrix traction forces in mutant microvessels. To assess changes in cell-
252 generated forces, we visualized the collagen matrix surrounding the microvessels through
253 reflectance imaging and compared the displacement of matrix before and after lysing ECs with
254 detergent (**Figure 6C-D**). Notably, we observed significantly lower matrix displacement in mutant
255 microvessels when compared to control (**Figure 6B-D**), indicating reduced traction forces in
256 *PIK3CA*^{E542K} microvessels.

257 *PIK3CA*^{E542K} *microvessels are unresponsive to flow interruption.*

258 To determine whether the slow-flow environment of native lesions potentiates VM progression,
259 we next investigated the effect of transitioning from flow to static culture of *PIK3CA*^{WT} and
260 *PIK3CA*^{E542K} microvessels by preconditioning microvessels with flow for 24 hrs then transitioning
261 to static conditions for the subsequent 24 hrs. After transition to static culture, *PIK3CA*^{WT} HUVECs
262 delaminated and detached into the apical lumen, resulting in gaps in the endothelium (**Figure**
263 **7A**). In contrast, *PIK3CA*^{E542K} HUVECs were insensitive to flow interruption, with no observable
264 delamination and the formation of tortuous, sprouted, and dilated microvessels that are akin to

265 mutant vessels cultured under flow conditions (**Figure 7B-C**). In all culture conditions,
266 *PIK3CA*^{E542K} microvessels contained approximately twice the number of cells and were
267 approximately 2-fold wider than *PIK3CA*^{WT} microvessels (**Figure 7C**). While *PIK3CA*^{E542K}
268 microvessels showed minimal effects from flow interruption, flow interruption in *PIK3CA*^{WT}
269 microvessels resulted in gaps covering approximately 6.5% of the vessel area (**Figure 7C**).
270 Similar lack of cell delamination and cellular invasion were observed in *PIK3CA*^{E542K} microvessels
271 cultured under fully static condition (**Figure S5A-C**). Collectively, these findings indicate that
272 constitutive PI3K activation renders ECs insensitive to vascular regression upon flow interruption
273 and may lead to improved survival and favorable expansion of mutant ECs in the no flow and
274 slow flow characteristics of PIK3CA-driven VMs.

275 *Basal-to-apical transmural flow exacerbates hypersprouting in PIK3CA mutant microvessels.*

276 In addition to luminal shear stress, venous and lymphatic ECs are subjected to draining
277 transmural flow. Hydrostatic and oncotic pressure differences across the vessel wall causes fluid
278 to extravasate from blood capillaries, resulting in the accumulation of interstitial fluid in the
279 surrounding matrix which is subsequently reabsorbed and collected by venous and lymphatic
280 vessels [38]. Therefore, in addition to experiencing low level of wall shear stress, venous and
281 lymphatic ECs are also subjected to fluid stresses arising from transmural drainage. To investigate
282 the effect of transmural flow on control HUVECs, *PIK3CA*^{WT}, and *PIK3CA*^{E542K} microvessels, we
283 cultured control or mutant HUVECs microfluidic devices that contain two parallel microvessels in
284 a shared collagen I hydrogel [39]. This two-channel configuration allows us to establish a pressure
285 gradient between the two microchannels to drive transmural flow into (draining vessel, basal-to-
286 apical flow) or out of (source vessel, apical-to-basal flow) a microvessel (**Figure 8A, Figure S6A**).
287 We observed increased HUVEC invasion, reminiscent of angiogenic sprouting [40], into the
288 subluminal collagen I hydrogel upon application of transmural flow in the basal-to-apical direction
289 in *PIK3CA*^{E542K} microvessels as compared to control HUVECs or *PIK3CA*^{WT} microvessels (**Figure**
290 **8A-C**). Consistent with previous reports [41-43], this increase in cell invasion primarily occurred
291 with the application of basal-to-apical, but not apical-to-basal transmural flow (**Figure 8A-B**).

292 *PIK3CA*^{E542K} *activation drives non-cell-autonomous sprouting in mosaic microvessels.*

293 Slow-flow VMs arise from sporadic somatic mutations, resulting in vascular lesions consisting of
294 endothelial cells with and without the driving mutations. The mosaic nature of vascular lesions
295 implies a role of non-cell autonomous signaling where mutated endothelial cells influence the
296 behavior of neighboring non-mutated cells to amplify lesion growth and progression. To determine
297 how *PIK3CA*^{E542K} HUVECs influence non-mutated HUVECs, we generated mosaic microvessels
298 containing HUVECs expressing histone *H2B-mCherry* and inducible *tet-ON-PIK3CA*^{E542K}. We
299 then applied basal-to-apical transmural flow and investigated whether doxycycline induced
300 expression of *PIK3CA*^{E542K} influenced sprouting and invasion behavior of control *H2B-mCherry*
301 HUVECs (**Figure 9A**). We found that doxycycline induction increased both the number of *H2B-*
302 *mCherry* and *PIK3CA*^{E542K} HUVECs located within sprouts (**Figure 9B**), indicating a non-cell-
303 autonomous effect of PI3K activation on sprouting angiogenesis. We further quantified the tip cell
304 distribution in mosaic sprouts and observed that *tet-ON-PIK3CA*^{E542K} and *H2B-mCherry* HUVECs
305 contributed to 40% and 60% of tip cells, respectively in untreated mosaic microvessels (**Figure**
306 **9C-D**). Doxycycline treatment drastically changed the proportion of control and mutant tip cells,
307 where *PIK3CA*^{E542K} HUVECs occupied 87% of the tips and *H2B-mCherry* HUVECs contributed
308 mostly as stalk cells in mosaic sprouts of doxycycline treated microvessels (**Figure 9C-D**).

Together, these results suggest that *PIK3CA*^{E542K} endothelial cells are more migratory and have a propensity to lead the sprouting and invasion of non-mutated endothelial cells.

We next determined whether the non-autonomous effect on sprouting is a result of matrix remodeling by *PIK3CA*^{E542K} HUVECs. Proteolytic degradation of the subluminal collagen matrix is known to be required for angiogenic sprout initiation and extension [44]. Previously, we described an increase in protease secretion and ECM degradation by *PIK3CA-mutant* HUVECs [19], and we thus hypothesized that ECM degradation and remodeling by *PIK3CA*^{E542K} HUVECs may prime *PIK3CA*^{WT} HUVECs for angiogenic sprouting. To test this hypothesis, we formed *PIK3CA*^{WT} and *PIK3CA*^{E542K} microvessels and lysed cells after 24 hrs, then reseeded the resulting channels with *PIK3CA*^{WT} HUVECs (**Figure 9E**). We then applied basal-to-apical transmural flow and quantified the number of sprouts formed in primed ECM (**Figure 9F**). We found that *PIK3CA*^{WT} HUVECs cultured in microvessels primed by *PIK3CA*^{E542K} HUVECs failed to reproduce the hypersprouting phenotype (**Figure 9F**). This finding suggests that changes in matrix architecture and mechanics caused by *PIK3CA*^{E542K} HUVECs are not sufficient to account for the etiopathology of VMs.

PIK3CA activation leads to increased endothelial cell and nuclear compliance.

Increased cell and nuclear compliance has been shown to promote 3D migration in various cell types [45], and we thus hypothesized that the hypersprouting observed in *PIK3CA*^{E542K} microvessels was driven by changes in cell and/or nuclear mechanical properties of *PIK3CA*^{E542K} HUVECs. To distinguish changes in cell intrinsic mechanics from tissue mechanics, we quantified cellular and nuclear deformation on a single cell basis using a microfluidic micropipette aspiration assay [46, 47] (**Figure 10, Figure S7**). The microfluidic device was designed to have two inlets allowing for the perfusion and loading of cells through the main channel. The main channel contains an array of 18 pockets with narrow constriction micropipette channels and are connected to an outlet port which is open to the atmosphere (**Figure S7**). A pressure of 7.0 kPa was applied to inlet 1 and 1.4 kPa to inlet 2, and both outlets are drained through constricted channels to atmospheric pressure (**Figure S7B**). Cells are initially trapped in larger pockets before deforming into 5 μm × 5 μm constricted channels under a fixed pressure gradient, and deformation was imaged via optical microscope for 2 minutes (**Figure 10B, Figure S7**). Interestingly, while untransduced HUVECs maintained cellular integrity for the duration of the experiment, *PIK3CA*^{WT} and *PIK3CA*^{E542K} endothelial cells were prone to fracture as the cells passed through the narrow constriction, with *PIK3CA*^{E542K} cells having the lowest probability of survival throughout the experiment (**Figure 10C**). The cytoplasm and nuclear protrusion length were measured as a function of time, and while the cytoplasm of *PIK3CA*^{WT} and *PIK3CA*^{E542K} HUVECs deformed similarly in response to the applied pressure gradient, both cell types demonstrated greater cytoplasmic deformation and cytoplasm fracture than untransduced HUVECs (**Figure 10C-D**). The nuclei of the three cell types deformed at different rates, with untransduced HUVEC nuclei experiencing the least deformation over time and *PIK3CA*^{E542K} expressing nuclei experiencing the greatest deformation (**Figure 10E**). Nuclear and cytoplasm viscoelastic properties were computed from the protrusion curves, as described previously [47]. Interestingly, *PIK3CA*^{E542K} and *PIK3CA*^{WT} HUVECs share similar cytoplasmic viscoelastic properties and are more compliant and less viscous than the cytoplasm of untransduced HUVECs (**Figure 10F**). The nuclei of *PIK3CA*^{E542K} HUVECs showed reduced elasticity as compared to the nuclei of *PIK3CA*^{WT} and untransduced HUVECs but exhibited the same viscous properties as *PIK3CA*^{WT} nuclei (**Figure 10G**). Thus, *PIK3CA*^{E542K} HUVECs were distinguished only by their reduced nuclear elastic modulus

compared to *PIK3CA*^{WT} HUVECs. Together, these results demonstrated increased cellular and nuclear compliance in PIK3CA-mutant ECs which may underlie dilation and overgrowth of venous and lymphatic vessels.

Discussion and conclusion

PIK3CA-driven VMs stereotypically present in soft tissues with low rates of perfusion [4, 48]. Here, using a series of engineering and microfluidic tools, we investigated the role of the biophysical microenvironment in the development of slow-flow vascular malformations to test the hypothesis that low hemodynamic shear stress potentiates lesion formation. Alignment and elongation of the cytoskeleton in the direction of flow is a hallmark of endothelial mechanotransduction [49], and laminar shear stress has been shown to regulate vascular barrier function locally and acutely [31, 50]. Furthermore, a lack of alignment and barrier function in response to hemodynamic shear stress is indicative of endothelial dysfunction [51]. Here, using both an orbital flow system to impart a range of shear stress magnitudes and a Hele-Shaw flow cell for unidirectional, laminar flow, we observed that HUVECs and LECs expressing a constitutively active PIK3CA-activating mutation fail to elongate and align in response to laminar shear stress (**Figures 1-2**). The lack of cell alignment was also reflected in a more isotropic distribution of microtubules and intermediate filaments in mutant cells (**Figures S3-S4**). Furthermore, the permeability of PIK3CA-mutant endothelial cells remained elevated even in the presence of physiologic shear stress (**Figures 1-2**). Together, these results suggest that dysfunctional mechanotransduction and resultant insensitivity to flow could be a key mechanism that underlies the dysregulated vascular networks characteristic of VMs (**Figure S8**).

We observed that *PIK3CA*^{E542K} microvessels generate lower net traction forces than *PIK3CA*^{WT} microvessels (**Figure 6**). Previous work has demonstrated that in multicellular systems, traction forces measured at cell-ECM interfaces are impacted by changes in cell-cell and cell-matrix adhesion [52], and that maturation of adherens junction complexes requires a balance of MLC-mediated cell-generated forces and Rac1 activity [53]. Previously, we identified that *PIK3CA* activating mutations result in excess Rac1 activity [19]. Here, we observed that expression of *PIK3CA*^{E542K} reduced MLC phosphorylation and recruitment of vinculin to adherens junction complexes, resulting in the discontinuity of junctional VE-cadherin and increased permeability (**Figure 3-4**). Together, these results suggest that pathophysiologic PI3K activation results in adherens junction instability through mechanical imbalances at cell-cell junctions, consistent with previous work demonstrating that PIK3CA signaling inhibits NUAK1-dependent phosphorylation of myosin phosphatase targeting-1 in ECs, leading to reduced overall actomyosin contractility [18]. Collectively, these results suggest that adherens junction instability and lack of maturation in response to hemodynamic signals render PIK3CA mutant cells prone to angiogenesis and could underlie the overconnected topologies characteristic of VMs.

Clinically, VMs are described as soft and compressible, and histologically they appear as a single layer of endothelial cells in enlarged vein-like channels with disorganized pericellular matrix [4]. To recapitulate the compliant ECM characteristic of tissues susceptible to VMs, we developed a 3D microfluidic model of vascular malformations and observed cellular signatures consistent with the clinical presentation of VMs, including irregular and dilated microvessels (**Figure 6**). In previous work, we performed a broad characterization of MMPs and fibrinolytic enzymes in conditioned media from wild type and mutant ECs, and we observed upregulation of MMP-1, which degrades collagen type I [19]. These results are consistent with the increased diameter of mutant microvessels (**Figure 6A-B**), and could contribute to the increased sprouting in response

399 to flow, as perfusion has been shown previously to regulate angiogenesis in an MMP-1-dependent
400 manner [54].

401 Previously, we have shown that reducing hemodynamic shear stress leads to rapid adherens
402 junction dissolution [31], and experiments conducted in developmental animal models have
403 demonstrated that reduction or interruption of flow induces vessel regression and network pruning
404 [55], which is thought to be essential for optimization of efficient delivery of oxygen and nutrients
405 [56, 57]. To recapitulate the hemodynamic signals associated with pruning, we exposed
406 microvessels to flow for 24 hrs, then interrupted flow and cultured microvessels in static conditions
407 for 24 hrs. Interestingly, PIK3CA mutant microvessels did not respond to flow interruption, and
408 mutant ECs remain attached and continue to grow under static culture conditions, whereas wild-
409 type ECs delaminate from the vessel wall (**Figure 7, Figure S5**). These results suggest that cells
410 expressing activating PIK3CA mutations are primed for survival in the unique hemodynamic
411 environment of slow-flow lesions, and that this survival results in a lack of pruning in response to
412 reduced or interrupted perfusion to allow VM progression in the slow-flow microenvironment.

413 Computational modeling and a limited number of experiments have demonstrated that changes
414 in vascular network topology modulate not only local wall shear stress but also luminal pressure
415 [58]. To determine whether gradients in fluid pressure could play a role in lesion formation, we
416 fabricated microfluidic devices to expose wild-type and mutant microvessels to transmural
417 pressure gradients. We observed that transmural pressure gradients and resultant flow in the
418 basal-to-apical direction results in increased sprouting and invasion of PIK3CA-mutant ECs as
419 compared to control microvessels (**Figure 8**). Previously, immature endothelial monolayers,
420 characterized by discontinuous junctional VE-cadherin, have been shown to sprout in response
421 to lower basal-to-apical pressure drops than mature monolayers with continuous pericellular VE-
422 cadherin [54], suggesting that the increased sprouting in PIK3CA-mutant ECs could be driven by
423 immature adherens junctions. Furthermore, basal-to-apical transmural flow has been shown to
424 synergize with VEGF gradients to increase angiogenic sprouting [42], and a recent study has
425 demonstrated increased paracrine VEGF-C signaling in *PIK3CA*-driven mosaic LM mouse model
426 [26]. Together, these results suggest that transmural pressure gradients and flow are a pro-
427 angiogenic stimulus that drives lesion elaboration and growth.

428 Permeability measurements and images of pericellular VE-cadherin (**Figures 1, 3**), suggest that
429 adherens junctions in mutant cells are immature and discontinuous. To relate the junctional
430 phenotypes to the dysfunctional response to shear stress, we investigated whether downstream
431 effector signaling modulated by key mechanosensory complexes that contain VE-cadherin [22,
432 23, 31] were differentially regulated in mutant cells. We first quantified the stability of VE-cadherin
433 intercellular adherens junctions using a pulse-chase approach and observed a significantly
434 reduced level of labeled VE-cadherin at cell-cell contacts (**Figure 4**). We then tested the
435 hypothesis that Src kinase, which is activated by the VE-cadherin/PECAM/VEGFR2
436 mechanosensory complex [23], is differentially phosphorylated by mutant cells. Interestingly, we
437 found that Src phosphorylation was similar in magnitude and temporal activation among
438 untransduced HUVEC, *PIK3CA*^{WT}, and *PIK3CA*^{E542K} cells (**Figure 4)**. Furthermore, closer
439 inspection of the pulse-chase staining of VE-cadherin reveals an increase in the intracellular
440 puncta of AF647-VE-cadherin, suggesting increased VE-cadherin internalization and recycling.
441 Previous work has established mature adherens junctions as sites of cytoskeletal organization
442 [59], that VE-cadherin is necessary for proper alignment of the cytoskeleton in response to shear
443 stress [60], and that pericellular VE-cadherin localization balances cell-generated forces

associated with cortical actin elaboration [53, 61]. Thus, our data suggest that hyperactive PIK3CA activity, driven by mutant expression, reduces adherens junction stability through increased VE-cadherin turnover, which results in defective coordination of cytoskeletal dynamics and resultant alignment in response to flow, but that sites of assembled VE-cadherin are capable of transducing flow responses as measured by Src phosphorylation. Future work will seek to corroborate these results and provide greater mechanistic insight through dynamic characterization of gene expression profiles and direct testing of mechanosensory complex assembly and stability through immunoprecipitation.

Previous studies have demonstrated that nuclear stiffness and deformability play a role in 3D cellular migration through dense collagen matrices and spatially constraining micropores [45, 62]. Using a microfluidic micropipette aspiration assay, we found that *PIK3CA*^{WT} and *PIK3CA*^{E542K} ECs exhibit increased cellular compliance compared to untransduced HUVECs (**Figure 10**) and that *PIK3CA*^{E542K} ECs have significantly more compliant nuclei than *PIK3CA*^{WT} ECs. The increased cellular and nuclear compliance in PIK3CA-mutant ECs may facilitate EC migration and sprout formation, potentially contributing to hypervascularization in VM lesions. Previous work has demonstrated a role of Akt in phosphorylating Lamin A/C, resulting in degradation in keratinocytes [63] and C2C12 myocytes [64]. Furthermore, *Lmna*$^{-/-}$ MEFs demonstrate increased nuclear deformation in a microfluidic micropipette aspiration assay similar to the one employed here [47]. These results are consistent with our observations that *PIK3CA*^{E542K} cells, which we have previously shown have increased p-AKT (Ser^{473}) as compared to GFP transduction control cells [19], are characterized by increased nuclear deformation (**Figure 10**). While the specific mechanisms that relate PIK3CA activation to nuclear compliance remain unclear, increased invasion of colorectal cancer cells expressing PIK3CA activating through 8 μm pores and through Matrigel has been observed [65]. Conversely, knockdown of PIK3CA in glioblastoma cells reduces invasion into Matrigel [66], collectively suggesting that PIK3CA-mediated changes in nuclear mechanics could underlie a wide variety of pathogenic processes.

In summary, our findings demonstrate a role of altered mechanotransduction and cell mechanics in PIK3CA-driven vascular malformations (**Figure 8**). These findings could potentially be leveraged for genetic diagnosis and treatment of vascular anomalies. Molecular genetic testing for VMs remains challenging as the lesions are mosaic, with only a small population of cells expressing the driving mutations. Therefore, these reported changes in cellular mechanics may potentially be used as a biomarker for the sorting and enrichment of mutated ECs from patient biopsies. Further, targeting the defective contractility and recalibrating the mechanotransduction in mutant endothelial cells could represent an avenue to reduce or regress lesion progression.

Materials and methods

Cell culture, cloning, and lentiviral transduction

HUVECs (Lonza) and juvenile HDLECs (Promocell) were cultured in endothelial growth medium (EGM)-2 growth medium (Lonza) in a humidified incubator at 37 ºC and 5% CO_2. HUVECs were used between passages 6 and 12. HDLECs were used between passage 3 and 7. Lentivirus generation and transduction of HUVECs with pHAGE-PIK3CAWT, pHAGE-PIK3CAE542K, and pLenti6-H2B-mCherry (Addgene, plasmid #89766, gift from Torsten Wittmann) were performed as previously described [19]. PIK3CAE542K cDNA was amplified from pHAGE-PIK3CAE542K (Addgene, plasmid # 116479, gift from G. Mills and K. Scott) and was subcloned into pCW57.1, a third-generation inducible lentiviral expression vector (Addgene, plasmid # 41393, gift from David Root). Q5-site directed mutagenesis (New England Biolabs) was performed on pHAGE-PIK3CAE542K to generate pHAGE-PIK3CAWT plasmid. All plasmids were expressed through lentiviral transduction. For lentiviruses generation, HEK-293T cells were transfected with pHAGE or pCW57.1 constructs, pSPAX2 plasmid, and pMD2.g plasmid (Adggen plasmid # 12260 and #12259, gifts from D. Trono) using calcium phosphate transfection method. Lentiviral supernatants were collected between 48 hours to 72 hours post transfection. Supernatants containing lentiviruses were filtered purified using 0.45 µm PES filters. Cytoplasmic GFP fluorescence signal through the expression of pHAGE-PIK3CAE542K-ires-GFP or pHAGE-PIK3CAWT-ires-GFP was used to measure transduction efficiency and lentivirus tittering assays were performed to determine the lowest concentration required to achieve >90% transduction efficiency in HUVECs. HUVECs expressing pCW57.1-tetON-PIK3CAE542K were selected with 2 µg/mL of puromycin (Corning) and 5 µg/mL of blasticidin (Fisher) in EGM-2, respectively for at least two cell passages. Doxycycline (Sigma, 10 µg/mL in EGM-2) was used to induce the expression of tet-ON-PIK3CA^{WT} or tet-ON-PIK3CA^{E542K}.

Hemodynamic shear stress via orbital shaking and 2D permeability assay

HUVECs were seeded at 0.15 x 10^6 cells per well in a 6-well plate (Corning Costar 6-well Clear TC-treated, Cat #3516) coated with 50 µg/mL of rat-tail derived type I collagen (Corning 354326) in 0.02 M acetic acid solution. Cells were allowed to adhere overnight prior to the application of orbital shaking. Fresh EGM-2 (2 mL) was added into each well prior to the application of orbital flow. Orbital flow was applied by culturing ECs for 3 days on an orbital shaker set to 200 rpm, which corresponds to a maximum wall shear stress of 15 Dyn/cm^2 [67]. Computational fluid dynamics (CFD) models verified with particle imaging velocimetry (PIV) demonstrate that a well of this geometry, fill volume, and rotational speed will generate periodic wall shear stresses with mean values spanning from 0.8 – 13 Dyn/cm^2 from near the center of the well to the outer edge, respectively [67]. For measurements of local changes in vascular permeability, 0.3 x 10^6 cells HUVECs were seeded in each well of a 6-well plate coated with 50 µg/mL of biotinylated-human fibronectin (Corning 354008) in PBS. Fibronectin biotinylation was performed with EZ-link-Sulfo-NHS-LC-Biotin (Thermo Fisher A39257) as described previously [68]. Briefly, 0.1 mg/mL of fibronectin in PBS was incubated with 0.5 mM of EZ-link-Sulfo-NHS-LC-Biotin for 30 min at room temperature. At the end of orbital flow culture, cells were incubated with 25 mg/mL Cy3-Streptavidin (Jackson Immuno Research Labs 016160084) in PBS containing calcium and magnesium (PBS++) for 2 minutes. After streptavidin labeling of exposed matrix, cells were rinsed once with PBS++ and were fixed with 4% paraformaldehyde (Electron Microscopy Sciences) in PBS++ for 15 min at room temperature. Permeability was measured by quantifying the streptavidin positive area using the default auto thresholding method in ImageJ.

524 *Hydrogel formation and cell seeding in microvessel microfluidic devices*

525 Microfluidic devices were fabricated as described in the *Supplementary Methods*. To improve
526 hydrogel adhesion to PDMS devices prepared by photolithography, 2 mg/mL dopamine
527 hydrochloride in 10 mM of pH 8.5 Tris HCl buffer (BioWorld) was pipetted into the hydrogel
528 chamber, incubated for 1 hr at room temperature, rinsed twice with DI-H_2O, left dry at room
529 temperature, and sterilized via UV for 20 min. Sterile 160 µm stainless steel acupuncture needles
530 (Llahsa Oms) were coated with 0.01% bovine serum albumin (BSA) in PBS for at least 30 min
531 prior to hydrogel injection. BSA-coated needles were inserted into each device, and 2.5 mg/mL of
532 rat tail-derived collagen I hydrogel was prepared and pipetted into the hydrogel chamber as
533 described previously [37], and allowed to polymerize at 37 ºC for 30 min prior to hydrating with
534 EGM-2. After 4 hrs of further incubation at 37 ºC, acupuncture needles were gently removed from
535 devices to form a cylindrical channel within the collagen I hydrogel. Needle inlets were sealed
536 with vacuum grease (Millipore Sigma) and fresh EGM-2 was added to the media ports of the
537 devices. Devices were kept on a rocker at 5 cycles/min at 37 ºC and 5% CO_2 for at least 12 hrs
538 prior to cell seeding to rinse and equilibrate the collagen I hydrogel [37]. To form microvessels,
539 HUVECs were resuspended at 0.3 x 10^6 cells/mL in EGM-2. Media was removed from both media
540 ports and gel filling pipette tips were used to aspirate and empty the hydrogel ports prior to
541 seeding. To promote pressure driven flow into the microchannel, 50 µL and 40 µL of cell
542 suspension were added to the inlet and outlet media ports, respectively. Devices were inverted
543 every minute for 8 min at room temperature, followed by incubating upside-down in a tissue
544 culture incubator for 6 minutes. Devices were subsequently inverted and incubated for an
545 additional 6 minutes in the incubator. After 20 min of seeding, devices were placed on a rocker
546 for at least 2 hours before changing EGM-2 media, which was subsequently changed daily.

547 *Transmural flow in two-channel devices*

548 Two-channel devices were used to apply transmural flow into or out of microvessels (**Figure S6**).
549 For the application of transmural flow, microvessels were first cultured on rocker (5 cycles per
550 minute at ± 30° angle) for 2 days. Media reservoirs were inserted into all four media ports and any
551 gaps between reservoirs and PDMS were sealed with vacuum grease. Pre-warmed EGM-2 was
552 added either to the empty or microvessel channel to apply a 20 mm H_2O hydrostatic pressure
553 driven transmural flow into or out of the microvessels, respectively. Microvessels were fixed 24
554 hours after the application of transmural flow.

555 *Microfluidic micropipette aspiration*

556 Microfluidic devices were fabricated as described in the *Supplementary Methods.* The
557 micropipette aspiration device was used to deform cells under an applied pressure gradient.
558 Untransduced HUVECs, $PIK3CA^{WT}$, and $PIK3CA^{E542K}$ cells were cultured as described previously
559 before being stained with Hoechst 3342 (10 mg/mL, Thermo Scientific) and CellMask Deep Red
560 plasma membrane stain (5 mg/mL, 1:2000 v/v, Invitrogen) for 10 min to stain the nucleus and
561 plasma membrane respectively. Stained cells were washed with PBS and allowed to recover in
562 EGM-2 for 30 minutes. Cells were then trypsinized, counted, and resuspended at a concentration
563 of 5,000,000 cells/mL in BSA (20 mg/mL in PBS) before being put on ice. Constant-pressure
564 microfluidic flow controllers ("Flow EZ," Fluigent) were used to apply flow to the opposing inlets at
565 constant pressures, creating flow from one inlet to the other using a known pressure gradient.
566 Two flow controllers were each connected to a dry air source and a power outlet. One controller
567 was used to drive stained and suspended cells from a 15 mL conical tube into one inlet of the

568 microfluidic device at a pressure of 7.0 kPa. A second controller was used to drive cell-free PBS
569 from a 15 mL conical tube into the second inlet of the microfluidic device at a pressure of 1.4 kPa.
570 The outlet port of the device was open to the atmosphere (**Figure S7**).

571 *Decellularization and reseeding of decellularized microvessels*

572 Fresh sterile decellularization solution (0.5% Triton with 50 mM NH_4OH in PBS) was prepared on
573 the day of decellularization. Microvessels were rinsed once with sterile PBS prior to
574 decellularization. After PBS wash, 100 µL of decellularization solution was added to the media
575 ports of each device. Devices were kept on a rocker at 37 ºC and 5% CO_2 for 15 min.
576 Decellularized devices were washed three times with PBS and residual DNA was digested via
577 treatment with 10 µg/mL of DNAseI (Sigma Aldrich, D4527) in PBS++ for 45 minutes at 37 ºC.
578 DNAseI treated devices were washed three times with PBS and were incubated overnight on a
579 rocker in fresh EGM-2 media. Devices were reseeded with *PIK3CA*^{WT} cells the next day as
580 described in the "Hydrogel formation and cell seeding" section. Basal-to-apical pressure driven
581 transmural flow was applied a day after reseeding as described above.

582 *Immunostaining*

583 Mouse Anti–VE-cadherin (F-8) was from Santa Cruz Biotechnology. Rabbit Anti-VE-cadherin
584 (ab33168) was from Abcam. Mouse Anti-Vinculin (hVIN-1) was from Sigma Aldrich. 4′,6-
585 Diamidino-2-phenylindole (DAPI), rhodamine phalloidin (1 mg/ml), Alexa Fluor 488 phalloidin (1
586 mg/ml), and Alexa Fluor–conjugated secondary antibodies were from Life Technologies. Unless
587 otherwise mentioned, for endpoint immunostaining, cells or microvessels were fixed in 4% PFA in
588 PBS++ for 20 minute at room-temperature. For microtubule staining, cells were fixed in 100%
589 Methanol for 3 minutes at -20 ºC. Fixed samples were subsequently washed and rehydrated with
590 PBS. For visualization of vinculin at focal adhesion, cells were subjected to mild permeabilization
591 using 0.1% Triton X-100 in 4% PFA. Cells were partially perm-fixed for 5 minutes prior to switching
592 to complete fixation in 4% PFA for 15 minutes at room-temperature. All samples were
593 permeabilized with 0.3% Triton X-100 (Millipore Sigma) for 30 minutes at room temperature and
594 non-specific antibody binding was blocked by treatment with 2% (w/v) BSA in PBS for an hour at
595 room temperature. Primary antibodies against VE-cadherin (1:200, v/v, F-8, Santa Cruz
596 Biotechnology; 1:250, v/v, ab33168, Abcam), vinculin (1: 400, v/v, hVIN-1, Sigma Aldrich), α-
597 tubulin (1:1000, v/v, DM1A, Cell Signaling), and vimentin (1:200, v/v, D21H3, Cell Signaling) were
598 diluted in 2% BSA blocking solution and applied overnight on a laboratory rocker at 4 ºC. Cells
599 and devices were subsequently rinsed three times over 15 min with PBS, and were incubated in
600 secondary antibodies (1:1000, v/v, goat anti-mouse or goat-anti rabbit immunoglobulin G
601 conjugated to Cy3 or Alexa Fluor 647, Thermo Fisher Scientific), Alexa Fluor 488 or rhodamine
602 phalloidin (1:200, v/v, Thermo Fisher Scientific), and DAPI (1:1000, v/v, Thermo Fisher Scientific)
603 diluted in blocking solution for an hour at room temperature. Labeled cells and devices were rinsed
604 three times over 15 min with PBS and were stored in 0.01% Sodium Azide solution diluted in PBS
605 until imaging. Orientation of actin fibers was quantitatively determined from images of phalloidin
606 using the FibrilTool plugin for ImageJ [69].

607 *Western blots*

608 Cell lysates were collected from cells cultured in complete media for 24 hours. Briefly, cells were
609 washed once with ice cold PBS and lysed on ice with radioimmunoprecipitation assay buffer (RIPA
610 buffer, Thermo Fisher Scientific) containing 1X HALT protease and phosphatase inhibitor (Thermo
611 Fisher Scientific). Lysates were homogenized by pulse-vortexing and clarified by centrifugation at

612 14,000 x g for 5 min at 4 ºC. The concentration of clarified lysates was quantified using Pierce
613 BCA Protein Assay (Thermo Fisher Scientific). Lysates were then reduced with NuPAGE LDS
614 reducing agent and dithiothreitol and denatured for 5 min at 100 ºC. Denatured proteins were
615 resolved in NuPAGE 4 to 12% bis-tris gradient gels (Thermo Fisher Scientific) and transferred to
616 iBlot2 PVDF ministack membranes. Membranes were blocked with SuperBlock Blocking Buffer
617 (Thermo Fisher Scientific) for an hour with rocking at room temperature and were incubated with
618 the following primary antibodies for overnight with rocking at 4 ºC: anti-phosphoSRC(Tyr416)
619 (1:1000, Cell Signaling Technology, #2101), anti-p110α (1:1000, Cell Signaling Technology,
620 #9272), anti-vinculin (1:10,000, Sigma-Aldrich, V9264), anti-VE-cadherin (1:1000, Santa Cruz,
621 SC9989), anti-Beta-catenin (1:1000, Cell Signaling Technology, #8480), anti-glyceraldehyde-3-
622 phosphate dehydrogenase (1:5000, Cell Signaling Technology, #2118), and anti-phospho-myosin
623 light chain 2 (Thr18/Ser19) (1:1000, Cell Signaling Technology, #3674). After overnight incubation
624 with primary antibodies, membranes were washed three times with TBS-T and were subsequently
625 incubated with horseradish peroxidase conjugated antibodies (1:10,000, v/v, diluted in 5% milk
626 (w/v)) for 1 hour with rocking at room temperature. Membranes were then washed three times
627 over a period of 15 min with TBS-T and were developed via chemiluminescence using either
628 SuperSignal West Femto Maximum Sensitivity Substrate reagent (Thermo Fisher Scientific) or
629 Clarity Western ECL reagent (BioRad). Images of western blots were quantified using ImageJ.

630 *VE-cadherin pulse-chase staining*

631 For pulse-chase experiment, HUVECs were seeded and subjected to orbital shaking as described
632 in the Methods section. After conditioning with orbital flow for 3 days, cells were incubated with
633 AF647-anti-VE-cadherin antibody (1:200, v/v, diluted in pre-warmed EGM-2 media, BD
634 Biosciences, #561567) for 30 minutes orbital shaking. Unbound antibody was removed with two
635 washes with pre-warmed EGM-2 media, and cells were cultured for additional 2 hours under
636 orbital shaking prior to fixing.

637 *Imaging for Microvessels and flow-conditioned cells*

638 Confocal z-stacks of microvessels (4 μm step size, captured from top to bottom of the
639 microvessels) were acquired with an Olympus FV3000 laser scanning confocal microscope with
640 a 10x U Plan S-Apo NA 0.4 air objective. Confocal z-stack images of cells (0.8 μm step size,
641 captured from top to bottom of the samples) stained for VE-cadherin, vinculin, and cytoskeletal
642 proteins were captured with a 30X U Plan S-Apo NA 1.05 silicon oil objective. Fluorescence
643 images of cells after orbital flow were captured at 10x magnification (10X U Plan Fluor NA 0.3 air
644 objective, Olympus) using an automated scanning stage on an Olympus wide-field microscope.
645 Briefly, the edge of a well of a 6-well plate was positioned over the objective, and a uniform
646 rectangular area from the edge to the middle of the well was selected. A focus map was generated
647 to include at least 10 focus points along the length of the rectangular area. The autofocus feature
648 was used to cycle through the focus map and set the z-focus for each imaging point used
649 throughout the area scan. Computational image processing is described in the *Supplementary*
650 *Methods*.

651 *Imaging for Microfluidic Micropipette Aspiration Assay*

652 Cell deformation into the micropipette channels was imaged using a timelapse acquisition on an
653 inverted widefield fluorescence microscope (Olympus IX83) with a white light source 20X/NA 0.45
654 objective. DAPI and Cy5 filters were used to image the nucleus and cytoplasm respectively, and
655 images were acquired every 2.935 seconds for a total acquisition time of 2.5 min. At the end of

656 each timelapse acquisition, deformed cells were cleared from the cell pockets by applying
657 pressure at the outlet port by pipette. Cleared pockets were then filled again by flowing cells during
658 the next acquisition period.

659 *Statistical analysis*

660 Graphs were generated and statistical analyses were performed in Prism 10 (GraphPad).
661 Unless otherwise mentioned, data were plotted as mean ± standard deviation of ≥3 experiments
662 and data points denote values from each cell or microvessel. Data set with normal distribution
663 were compared with two-tailed Student's test and one-way ANOVA followed by Tukey's post hoc
664 test. Kruskal-Wallis test followed by Dunn's multiple-comparison was used for comparison of
665 non-Gaussian distributed data. Two-way ANOVA followed by Šidák's test was used for
666 comparison of more than two variables.

667

668 **Figures and captions**

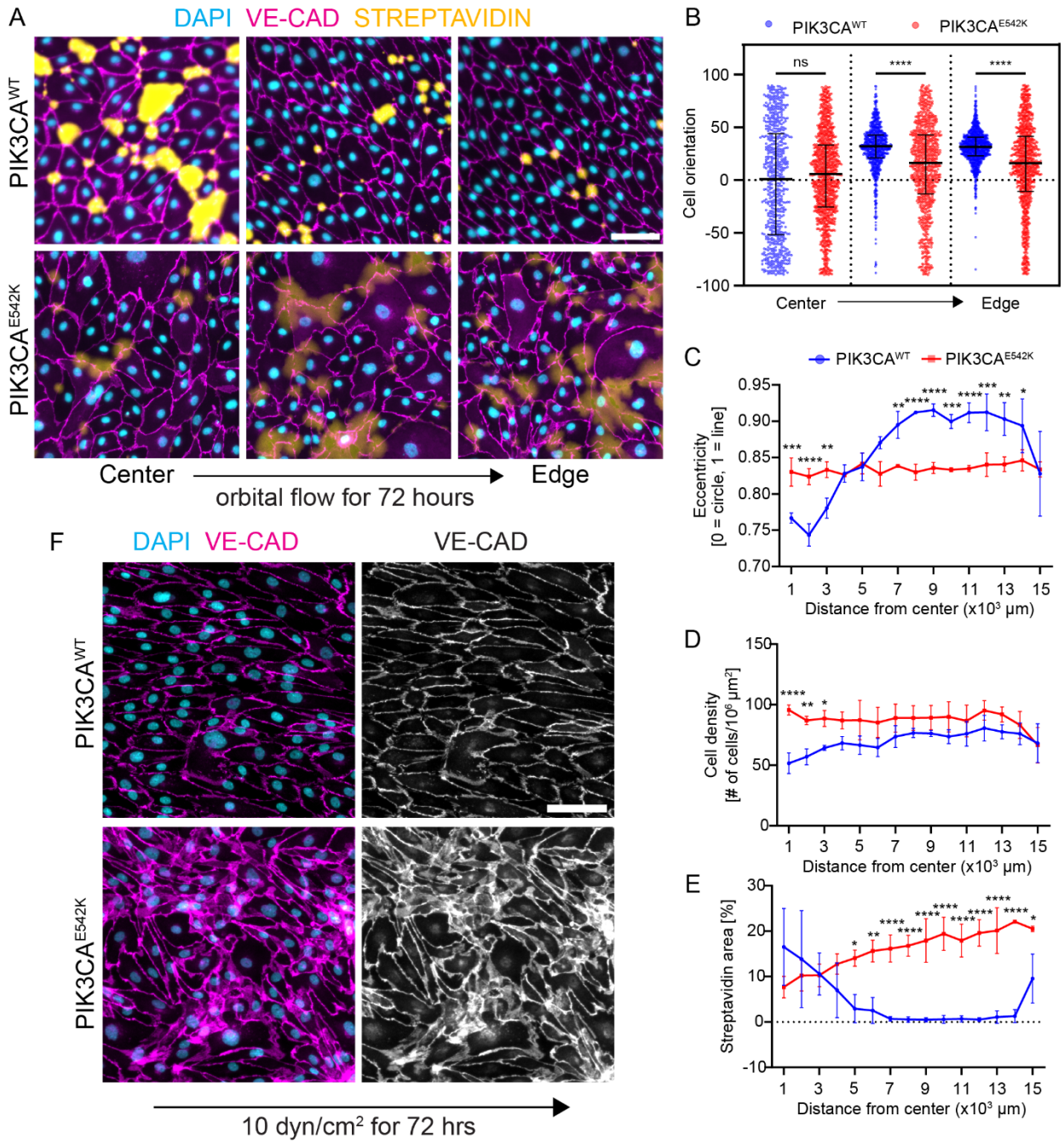

669

670 **Figure 1. Constitutive PI3K activation impedes shear stress-induced endothelial cell**
671 **alignment and vascular barrier function.** (**A**) Representative images of *PIK3CA^WT* and
672 *PIK3CA^E542K* HUVECs cultured on biotinylated fibronectin for 72 hr under orbital shaking
673 conditions. Cells were labeled with DAPI (cyan) and VE-cadherin (magenta). Monolayer
674 permeability was assessed through streptavidin labeling (yellow). Scale bar = 10 µm. (**B**)
675 Quantification of cellular orientation in the central, middle, or outer edge region of the well after
676 exposure to orbital shaking (n = 3; mean ± s.d., Kruskal-Wallis test followed by Dunn's test). (**C**)
677 Quantification of cellular eccentricity as a function of radial distance from the center of the well for

678 *PIK3CA*^{WT} and *PIK3CA*^{E542K} HUVECs (n = 3; mean ± s.d., two-way analysis of variance (ANOVA)
679 followed by Šidák's test). (**D**) Quantification of cell density as a function of radial distance from the
680 center of the well for PIK3CA^{WT} and PIK3CA^{E542K} HUVEC (n = 3; means ± s.d., two-way ANOVA
681 followed by Šidák's test). (**E**) Quantification of streptavidin intensity as a function of radial distance
682 from the center of the well for *PIK3CA*^{WT} and *PIK3CA*^{E542K} HUVECs (n = 3; mean ± s.d., two-way
683 ANOVA followed by Šidák's test). (**F**) Representative images of *PIK3CA*^{WT} and *PIK3CA*^{E542K}
684 HUVECs exposed to 10 dyn/cm^2 laminar shear stress in a Hele-Shaw flow cell. Scale bar = 10
685 µm. *p< 0.05, **p< 0.01, ***p< 0.001, ****p< 0.0001 for all plots.

686

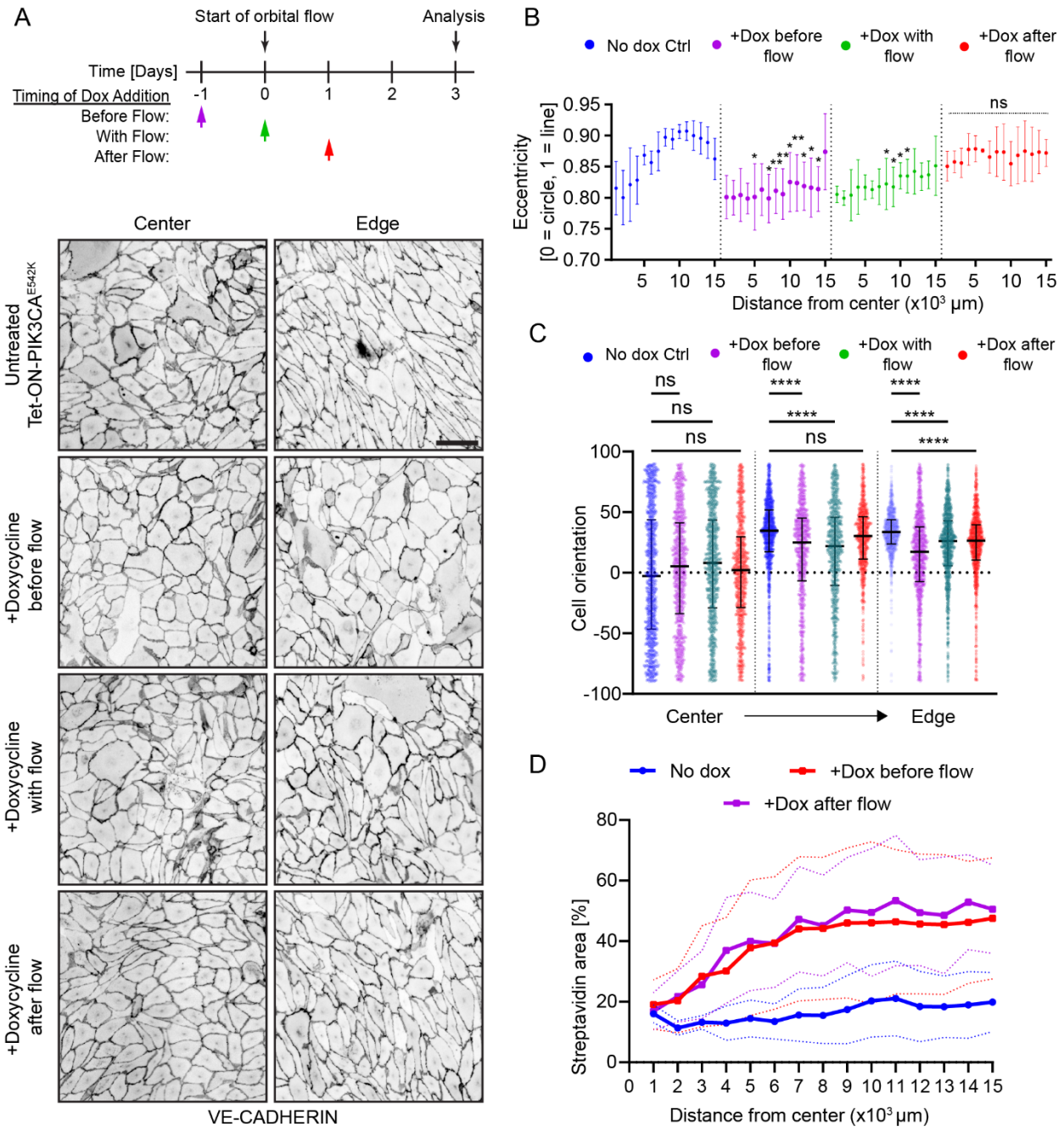

Figure 2. Preconditioning with shear stress prior to the induction of *PIK3CA^{E542K}* expression restores shear stress-mediated EC alignment but not barrier function. (**A**) Schematic of experimental workflow and representative images of VE-cadherin staining in control cells and cells where expression of *PIK3CA^{E542K}* was induced 24 hr before flow, at the onset of flow, or 24 hr after flow. Images were captured near the center of the well or near the outer edge of the well. Scale bar = 10 µm. (**B**) Quantification of cellular eccentricity as a function of radial distance for control cells as well as for cells induced with doxycycline 24 hr before flow, at the onset of flow, or 24 hr after flow (n = 3; mean ± s.d., two-way ANOVA followed by Šidák's test).

697 (**C**) Quantification of cellular orientation in the central, middle, or outer region of the well for cells
698 induced with doxycycline 24 hr before flow, at the onset of flow, or 24 hr after flow (n = 3; mean ±
699 s.d., Kruskal-Wallis tests followed by Dunn's test). (**D**) Quantification of streptavidin area as a
700 function of radial distance from the center of the well for control cells, cells induced with
701 doxycycline 24 hr before flow, and cells induced with doxycycline 24 hr after flow (n = 3; mean ±
702 s.d. (dotted lines), ANOVA followed by Dunnett test). *p< 0.05, **p< 0.01, ***p< 0.001, ****p<
703 0.0001 for all plots.

704

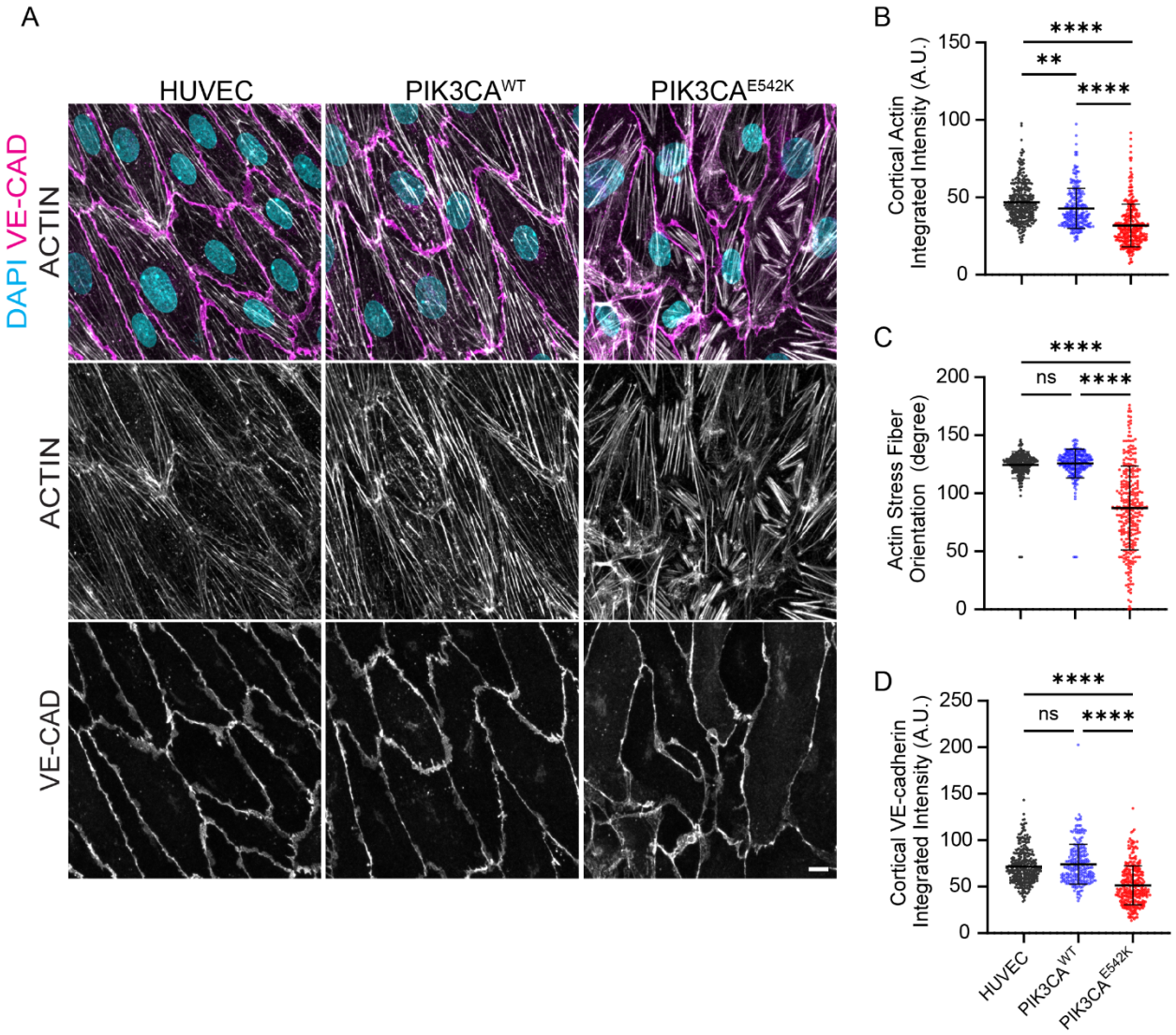

705
706 **Figure 3. Loss of stress fiber alignment, reduced cortical actin formation, and decreased**
707 **VE-cadherin accumulation at cell-cell contacts in *PIK3CA^{E542K}* endothelium.** (**A**)
708 Representative confocal images of untransduced HUVECs, *PIK3CA^{WT}*, and *PIK3CA^{E542K}*
709 HUVECs stained for DAPI (blue), actin (grey), and VE-cadherin (magenta). Cells were cultured
710 under orbital flow for 72 hours. Scale bar = 10 µm. (**B**) Quantification of the integrated intensity
711 of actin fluorescence signal at cell-cell contacts (n = 320 untransduced HUVECs, 244 *PIK3A^{WT}*

712 and 297 *PIK3CA*^{E542K} cells; mean ± s.d., one-way ANOVA followed by Tukey's test). (**C**) Angular
713 distribution of stress fiber orientation in flow-conditioned untransduced HUVECs, *PIK3CA*^{WT},
714 and *PIK3CA*^{E542K} HUVECs (n = 324 untransduced HUVECs, 248 *PIK3A*^{WT} and 296 *PIK3CA*^{E542K}
715 cells; mean ± s.d., one-way ANOVA followed by Kruskal-Wallis test). (**D**) Quantification of
716 endogenous VE-cadherin fluorescence signal at cell-cell contacts (n = 320 untransduced
717 HUVECs, 244 *PIK3A*^{WT} and 297 *PIK3CA*^{E542K} cells; mean ± s.d., one-way ANOVA followed by
718 Tukey's test).

719

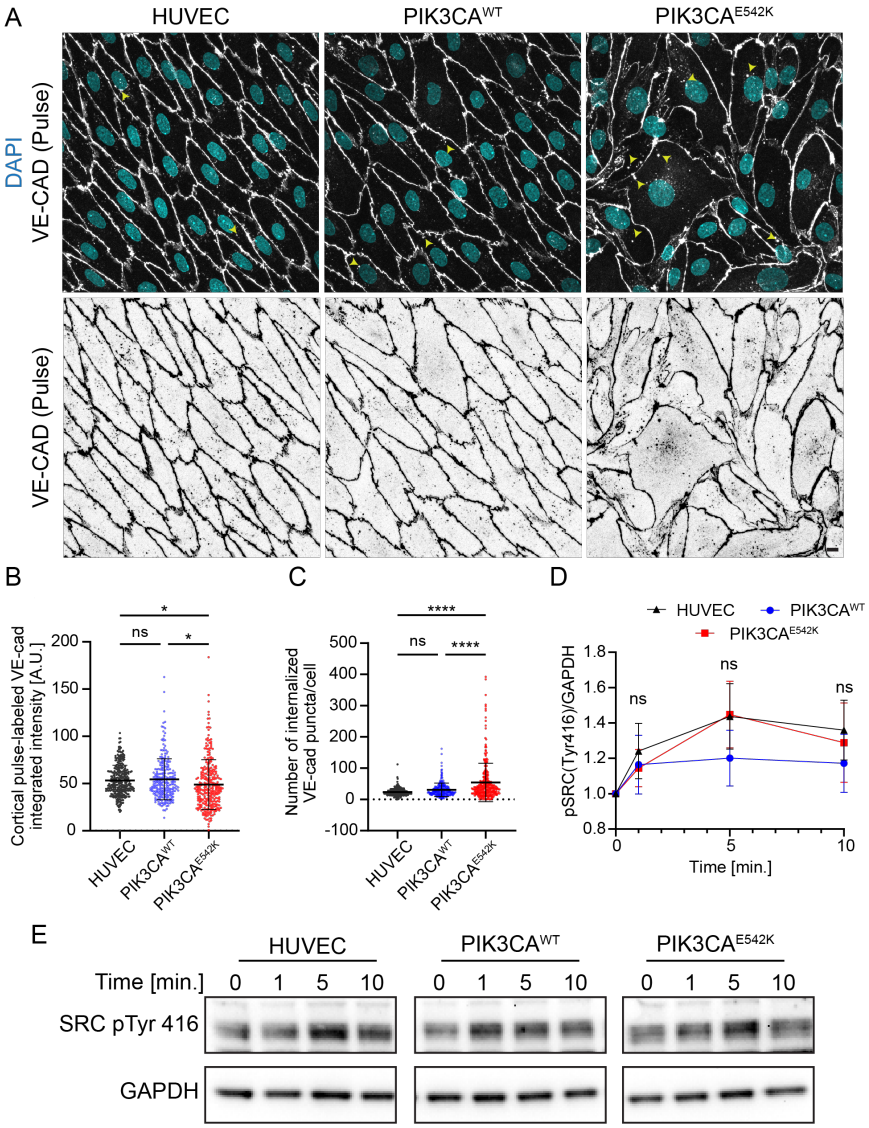

720

721 **Figure 4. Increased junctional VE-cadherin turnover with normal shear-stress induced**
722 **SRC phosphorylation in mutant *PIK3CA*^{E542K} ECs.** (**A**) Representative confocal images of
723 untransduced HUVECs, *PIK3CA*^{WT}, and *PIK3CA*^{E542K} HUVECs, where the surface-pool of VE-
724 cadherin (grey) was pulse-labeled with a fluorescently conjugated VE-cadherin antibody prior to
725 fixation and permeabilization. Unbound antibodies were washed, and cells were fixed and
726 stained with DAPI (blue) after a 2-hour chase period with media. Yellow arrowheads indicate

727 internalized pulse-labeled VE-cadherin puncta. Scale bar = 10 μm. (**B**) Quantification of pulse-
728 labeled VE-cadherin intensity at cell-cell contacts.junctions. (**C**) Quantification of the number of
729 VE-cadherin-positive puncta per cell (n = 316 untransduced HUVECs, 245 *PIK3A*^{WT} and 294
730 *PIK3CA*^{E542K} cells; mean ± s.d., one-way ANOVA followed by Tukey's test). (**D**) Changes in
731 phospho-SRC(Y416) (active-Src) level in untransduced HUVECs, *PIK3CA*^{WT}, and *PIK3CA*^{E542K}
732 HUVECs in response to the application orbital flow (n = 3; mean ± s.d., two-way ANOVA
733 followed by Tukey's test). (**E**) Representative western blot analysis of phospho-SRC(Y416)
734 levels in HUVECs, *PIK3CA*^{WT}, and *PIK3CA*^{E542K} HUVECs subjected to laminar shear stress
735 through orbital shaking for the indicated time points.

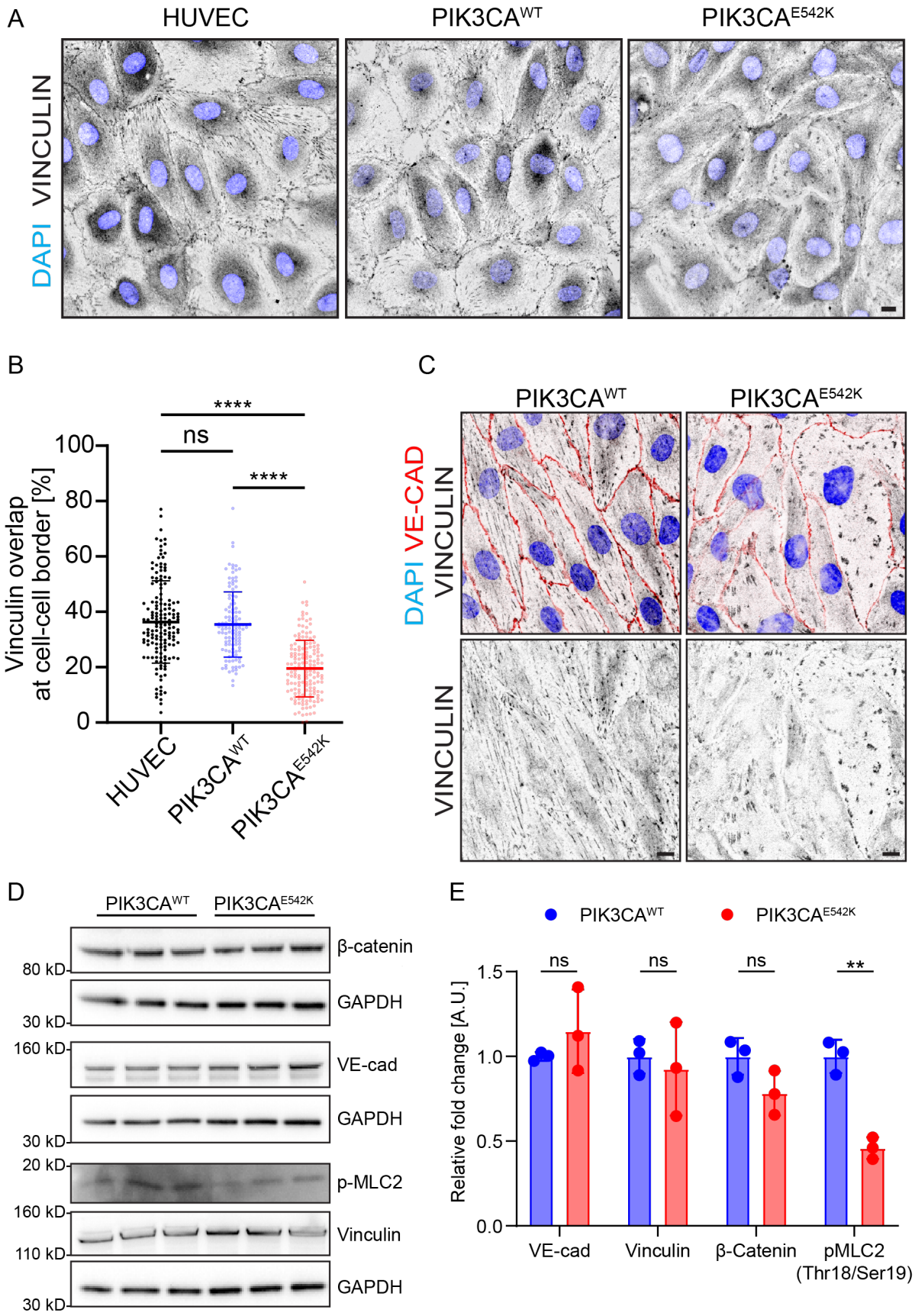
A
HUVEC
PIK3CA^WT
PIK3CA^E542K
DAPI VINCULIN
B
Vinculin overlap at cell-cell border [%]
100
80
60
40
20
0
****
ns
****
HUVEC
PIK3CA^WT
PIK3CA^E542K
C
PIK3CA^WT
PIK3CA^E542K
DAPI VE-CAD
VINCULIN
VINCULIN
D
PIK3CA^WT
PIK3CA^E542K
β-catenin
80 kD
GAPDH
30 kD
160 kD
VE-cad
GAPDH
30 kD
20 kD
p-MLC2
160 kD
Vinculin
110 kD
GAPDH
30 kD
E
PIK3CA^WT
PIK3CA^E542K
Relative fold change [A.U.]
1.5
1.0
0.5
0.0
ns
ns
ns
**
VE-cad
Vinculin
β-Catenin
pMLC2 (Thr18/Ser19)

736

737 **Figure 5. Loss of junctional vinculin recruitment in *PIK3CA*^{E542K} endothelium**. (**A**)
738 Representative confocal images of untransduced HUVECs, *PIK3CA*^{WT} and *PIK3CA*^{E542K}
739 HUVECs stained for vinculin (grey), and DAPI (blue). Scale bar = 10 µm. (**B**) Quantification of
740 percent vinculin area at cell-cell contacts (n = 119 untransduced HUVECs, 157 *PIK3A*^{WT} and
741 156 *PIK3CA*^{E542K} cells; mean ± s.d., one-way ANOVA followed by Tukey's test). (**C**)
742 Representative confocal images of vinculin localized at focal adhesions in flow-conditioned
743 *PIK3CA*^{WT} and *PIK3CA*^{E542K}. Cells were partially permeabilized during fixation and stained for
744 DAPI (blue) VE-cadherin (red) and vinculin (grey). Scale bar = 10 µm. (**D**) Western blots and (**E**)
745 quantification for β-catenin, VE-cadherin, phospho-myosin light chain 2, and vinculin level in
746 *PIK3CA*^{WT} or *PIK3CA*^{E542K} cells (n = 3; mean ± s.d., two-tailed unpaired t-test). *p< 0.05, **p<
747 0.01, ***p< 0.001, ****p< 0.0001 for all plots.

748

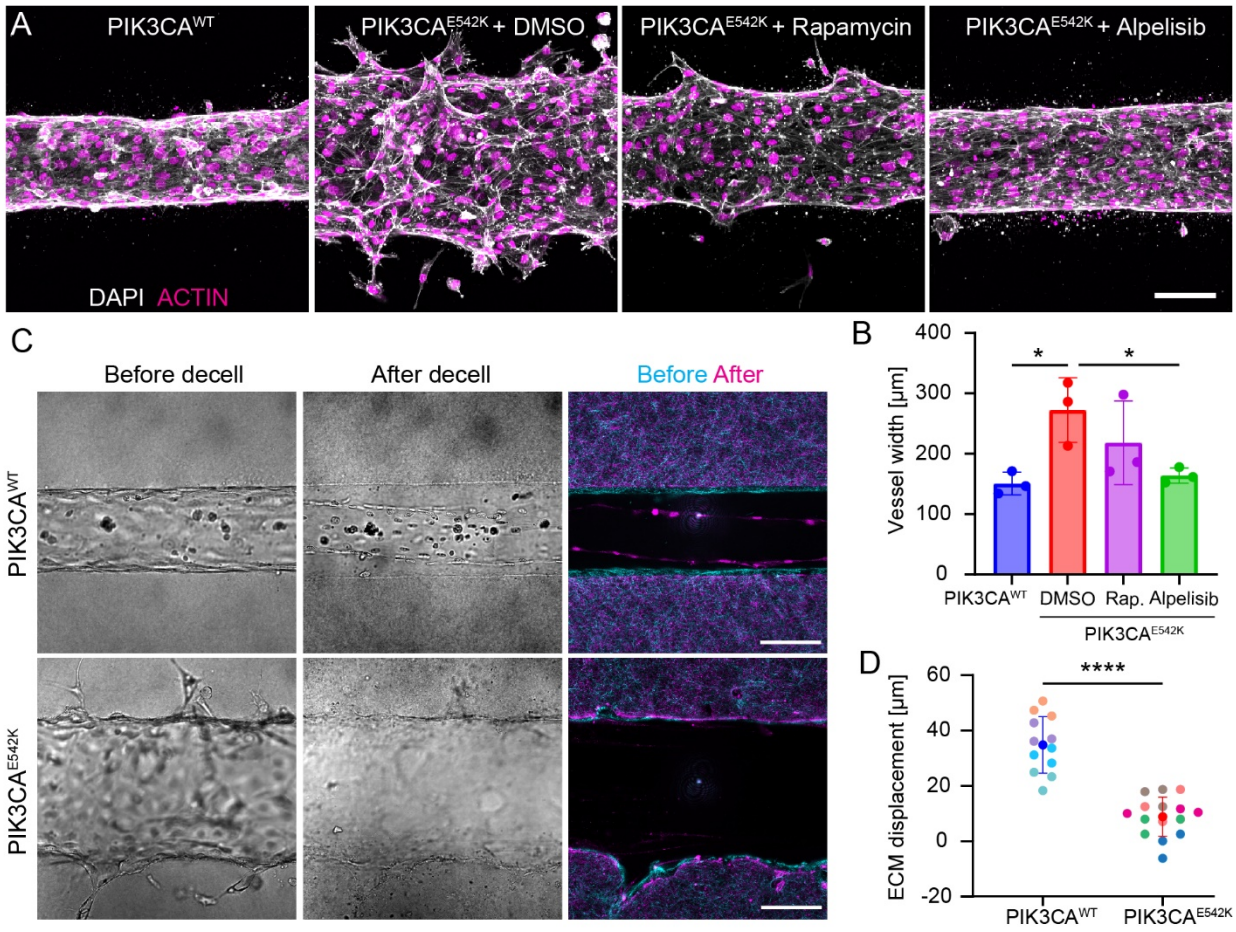

Figure 6. *PIK3CA^{E542K}* ECs form dilated microvessels with increased sprouting and reduced traction forces. (**A**) Representative confocal images (maximum intensity projections) of *PIK3CA^{WT}* and *PIK3CA^{E542K}* microvessels treated with DMSO, 1 µM alpelisib, or 1 µM rapamycin. Scale bar = 100 µm. (**B**) Quantification of vessel width in *PIK3CA^{WT}* microvessels or *PIK3CA^{E542K}* microvessels treated with DMSO load control, rapamycin (rap.), or alpelisib (n = 3; mean ± s.d., one-way ANOVA followed by Tukey test). (**C**) Representative phase contrast (grey) and confocal reflectance (cyan and magenta) images of *PIK3CA^{WT}* and *PIK3CA^{E542K}* microvessels before and after decellularization. (**D**) Quantification of subluminal ECM displacement before and after decellularization of *PIK3CA^{WT}* or *PIK3CA^{E542K}* microvessels (n ≥ 4 microvessels, 3 measurements per microvessel; data points from same devices are color-matched; mean ± s.d., two-tailed unpaired t-test). *p< 0.05, **p< 0.01, ***p< 0.001, ****p< 0.0001 for all plots.

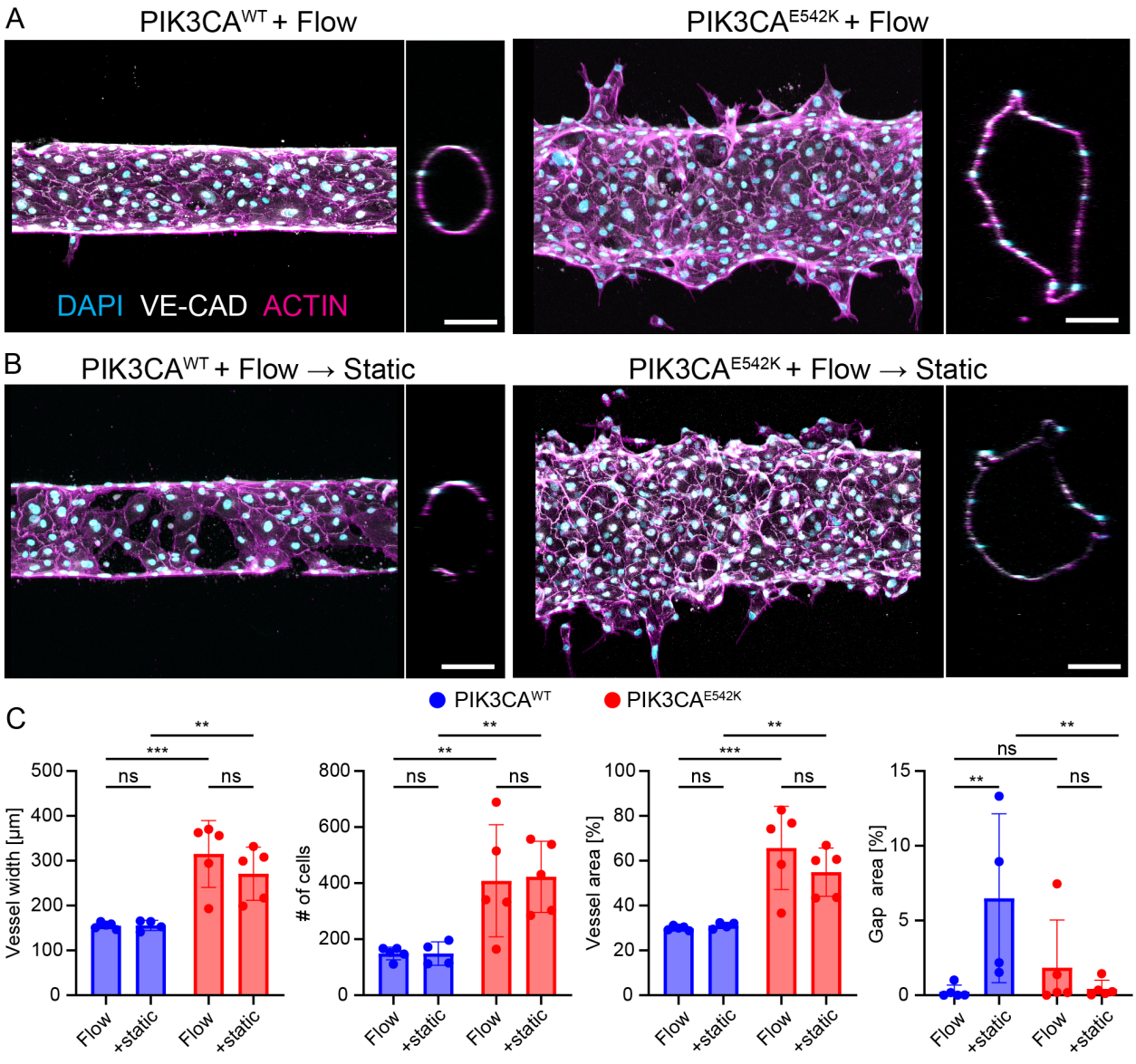

Figure 7. *PIK3CA^{E542K}* microvessels are unresponsive to flow interruption. (**A**) Representative images of microvessels generated from *PIK3CA^{WT}* and *PIK3CA^{E542K}* HUVECs. Microvessels were exposed to continuous rocking 48 hr and stained for DAPI (cyan), VE-cadherin (white), and F-actin (magenta). Scale bars = 100 µm. (**B**) Representative images of *PIK3CA^{WT}* and *PIK3CA^{E542K}* microvessels exposed to 24 hr rocking followed by 24 hr static conditions and stained for DAPI (cyan), VE-cadherin (white), and F-actin (magenta). Scale bars = 100 µm. (**C**) Quantification of vessel width, number of cells, vessel area, and gap area for *PIK3CA^{WT}* and *PIK3CA^{E542K}* microvessels exposed to either continuous or interrupted flow (n ≥ 4; mean ± s.d., two-way ANOVA). *p< 0.05, **p< 0.01, ***p< 0.001, ****p< 0.0001 for all plots.

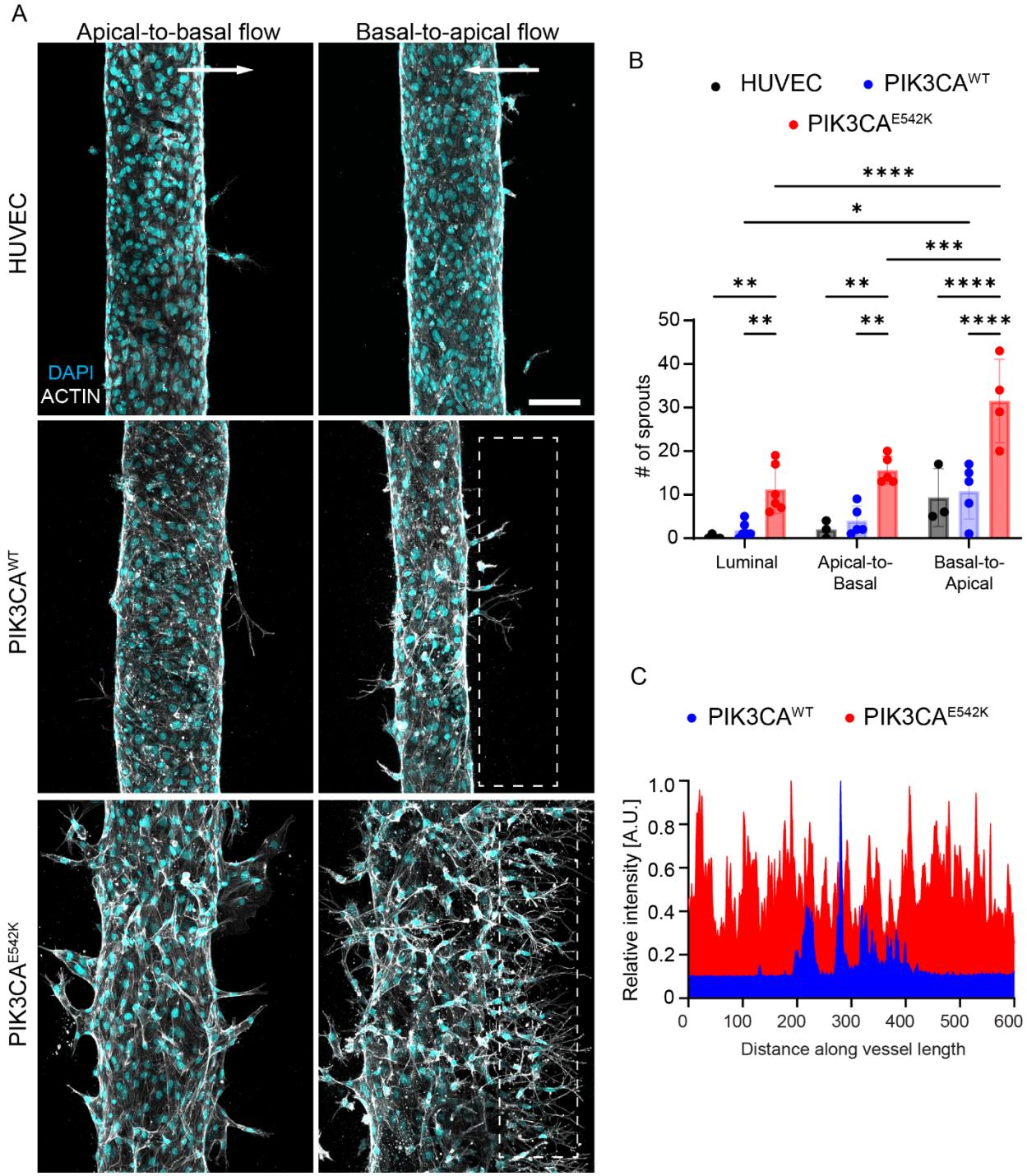

775

776 **Figure 8. Basal-to-apical transmural flow exacerbates hypersprouting in PIK3CA mutant**
777 **microvessels.** (**A**) Representative images of HUVEC, *PIK3CA*^{WT} and *PIK3CA*^{E542K} microvessels
778 exposed to continuous rocking for 48 hr and subsequently subjected to apical-to-basal (source)
779 or basal-to-apical (sink) transmural flow for 24 hr. Scale bar = 100 µm. (**B**) Quantification of
780 number of spouts in microvessels exposed to either luminal, apical-to-basal, or basal-to-apical
781 flow (n ≥ 3; mean ± s.d., two-way ANOVA followed by Tukey test). (**C**) Fluorescence intensity
782 profiles of actin channel were used to quantify number of sprouts in *PIK3CA*^{WT} or *PIK3CA*^{E542K}

783 microvessels. Dashed white boxes indicate where intensity profiles were extracted. *p< 0.05, **p<
784 0.01, ***p< 0.001, ****p< 0.0001 for all plots.

785

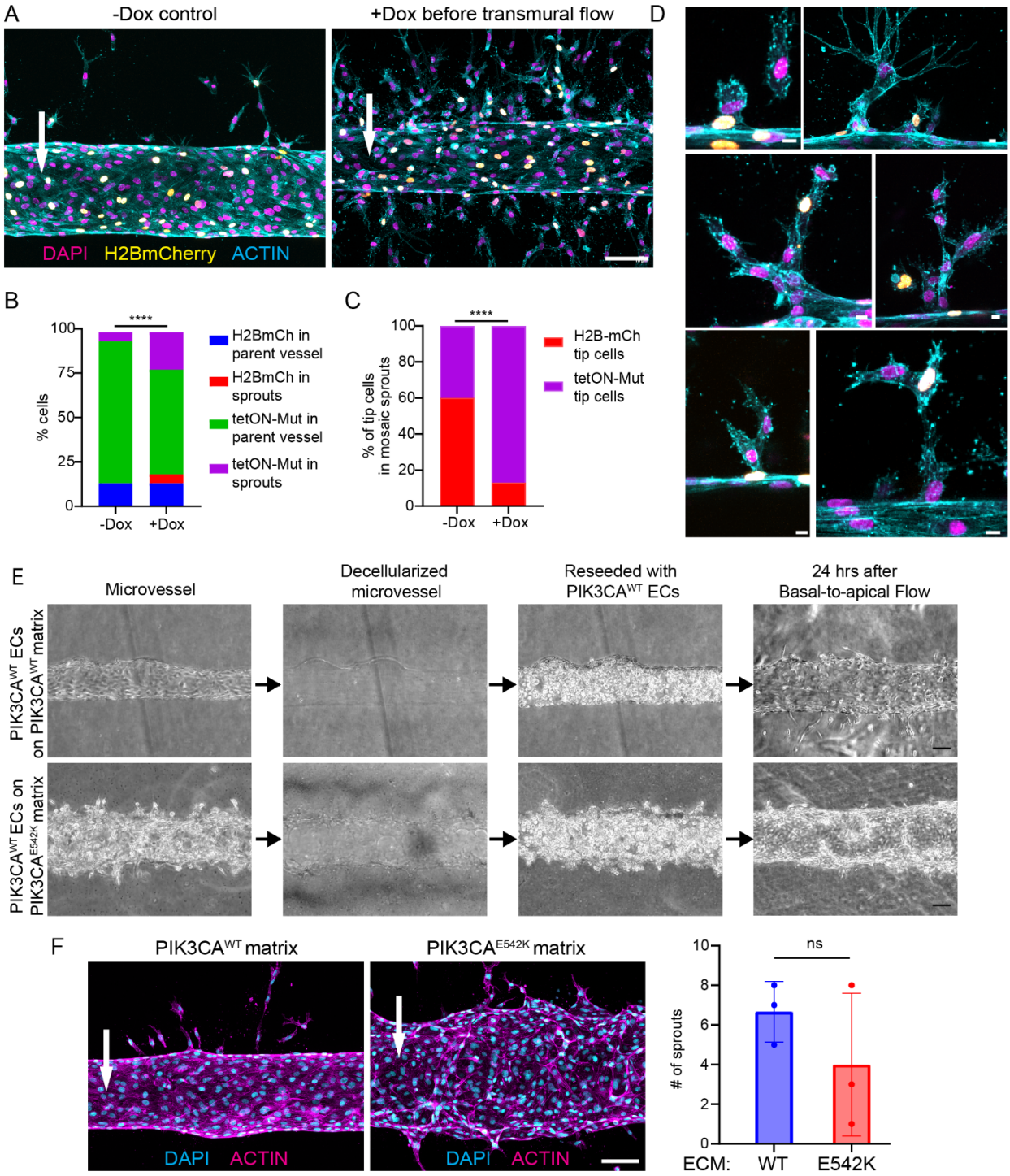

786

787

Figure 9. Mosaic co-culture of HUVECs with PIK3CA^{E542K} ECs resulted in increased sprouting of non-mutated HUVECs. (**A**) Representative images of mosaic microvessels generated using HUVECs expressing H2BmCherry and inducible tet-ON-PIK3CA^{E542K}. Microvessels were first exposed to continuous rocking 48 hr and then were subjected to basal-to-apical transmural flow for the next 24 hrs. PIK3CA^{E542K} expression was induced upon the application of transmural flow. Scale bar = 100 μm. (**B**) Quantification of the distribution of H2BmCherry and tet-ON-PIK3CA^{E542K} cells in mosaic vessels that were subjected to basal to apical transmural flow (n ≥ 3; chi-square test). (**C**) Quantification of percent H2BmCherry and tet-ON-PIK3CA^{E542K} tip cells in mosaic sprouts (n = 5 control and 15 doxycycline treated mosaic sprouts; chi-square test). (**D**) Images of mosaic H2BmCherry (yellow) and tet-ON-PIK3CA^{E542K} sprouts stained for DAPI (magenta) and actin (cyan). Scale bar = 10 μm. (**E**) Decellularized *PIK3CA^{WT}* and *PIK3CA^{E542K}* microvessels were reseeded with *PIK3CA^{WT}* HUVECs. Reseeded microvessels were subjected to basal-to-apical transmural flow for 24 hr. Scale bar = 100 μm. (**F**) Representative confocal images and number of sprout quantifications of transmural flow conditioned *PIK3CA^{WT}* microvessels cultured on extracellular matrix modified by control or mutant cells. Scale bar = 10 μm. (n = 3; mean ± s.d., unpaired two-tailed t-test).

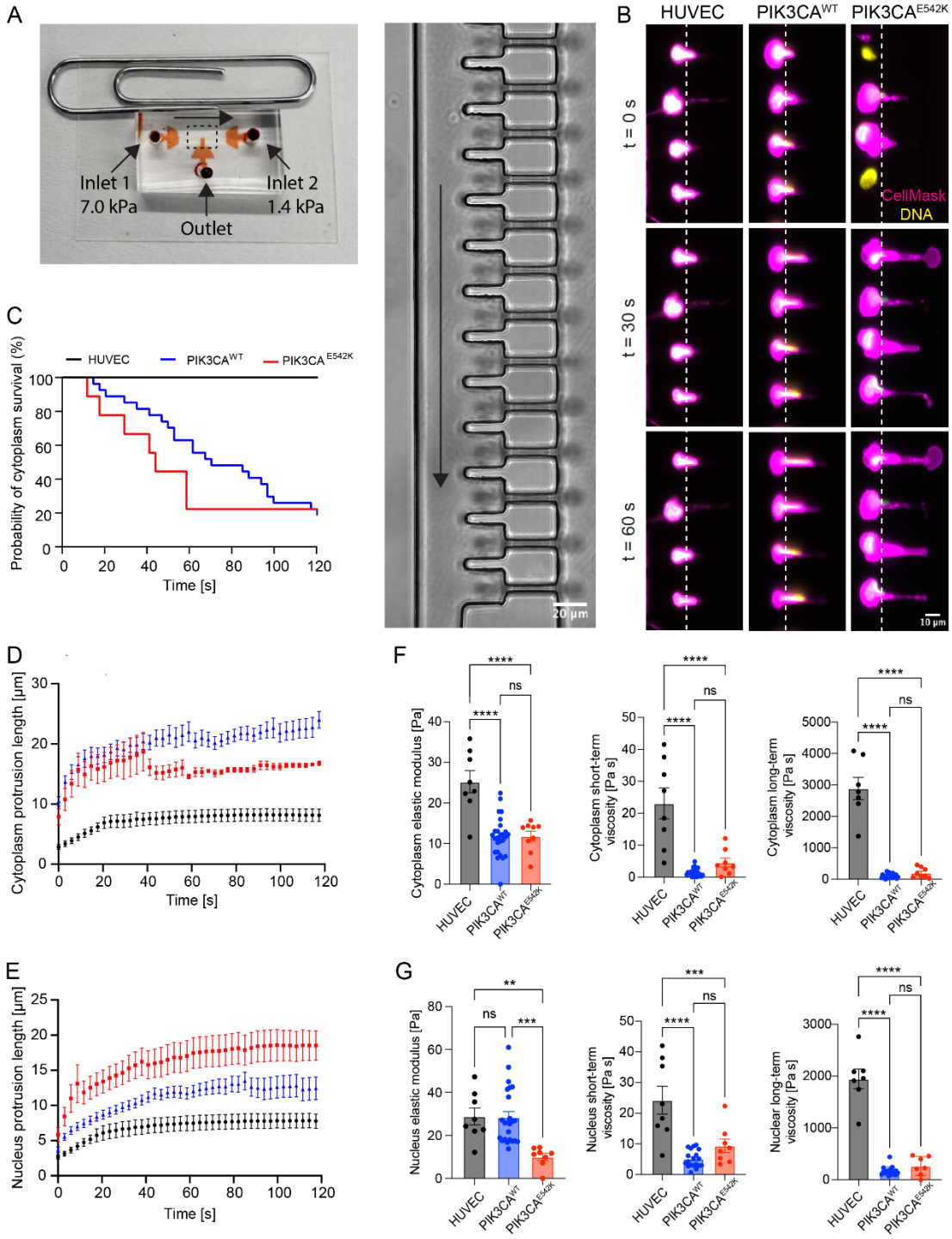
A
Inlet 1
7.0 kPa
Inlet 2
1.4 kPa
Outlet
20 µm
B
HUVEC
PIK3CA^WT
PIK3CA^E542K
t = 0 s
t = 30 s
t = 60 s
CellMask
DNA
10 µm
C
HUVEC
PIK3CA^WT
PIK3CA^E542K
Probability of cytoplasm survival (%)
Time [s]
D
Cytoplasm protrusion length [µm]
Time [s]
E
Nucleus protrusion length [µm]
Time [s]
F
Cytoplasm elastic modulus [Pa]
Cytoplasm short-term viscosity [Pa s]
Cytoplasm long-term viscosity [Pa s]
G
Nucleus elastic modulus [Pa]
Nucleus short-term viscosity [Pa s]
Nuclear long-term viscosity [Pa s]
ns
****
***
**

Figure 10. Altered cytoplasmic and nuclear mechanical properties of single cells expressing *PIK3CA*^{WT} or *PIK3CA*^{E542K} activating mutations. (**A**) An image of the microfluidic micropipette aspiration device labeled with an outlet and two inlets at differential pressures causing a flow vector between the two inlets. A magnified image depicts the dashed area, showing the array of pockets and constriction channels which trap and deform flowing cells under a constant applied pressure gradient. (**B**) Time-lapse images of nucleus (Hoechst) and cytoplasm (CellMask) deformation of untransduced HUVECs and endothelial cells expressing *PIK3CA*^{WT} or *PIK3CA*^{E542K} activating mutations. (**C**) Percentage of HUVECs that withstood deformation, as measured by the number of endothelial cells with intact cytoplasm after passage through the constriction channel relative to the total number of cells that entered the channels. (**D**) Protrusion length over time of endothelial cell cytoplasm into the constriction channels (mean ± s.e.m.). (**E**) Quantification of nuclear deformation over time of endothelial cells into constriction channels (mean ± s.e.m.). (**F**) Quantification of viscoelastic properties of the cytoplasm of endothelial cells (mean ± s.e.m., one-way ANOVA). (**G**) Elastic modulus, short-term viscosity, and long-term viscosity of the nuclei of HUVECs and endothelial cells expressing *PIK3CA*^{WT} or *PIK3CA*^{E542K} activating mutations (mean ± s.e.m., one-way ANOVA).

Acknowledgements

This work was funded by the National Institute of Health (R35GM142944), by the American Heart Association (CDA857738), and by research grants from the CLOVES Syndrome Community and the Lymphatic Malformation Institute. W.Y.A. is supported by grant from the CLOVES Syndrome Community. C.P.W. and E.L.D. are supported by a training fellowship from the Integrative Vascular Biology Training Program (T32HL69768), C.P.W. is supported by an American Heart Association predoctoral fellowship (24PRE1192185), and E.L.D. is supported by a Ruth L. Kirchstein predoctoral individual fellowship (F31HL162462). E.M. acknowledges support from an NIH training fellowship (T32GM135128). We thank Bob Geil for advice and help with microfabrication. The fabrication of microfluidic devices was performed in the Chapel Hill Analytical and Nanofabrication Laboratory (CHANL), a member of the North Carolina Research Triangle Nanotechnology Network (RTNN), which is supported by the National Science Foundation (ECCS-2025064), as part of the National Nanotechnology Coordinated Infrastructure (NNCI).

Author Declarations

Conflict of Interest

The authors have no conflicts to disclose.

Ethics Approval

Ethics approval is not required.

Data Availability

The data that support the findings of this study are available from the corresponding author upon reasonable request.

References

[1] K. Zenner, C.V. Cheng, D.M. Jensen, A.E. Timms, G. Shivaram, R. Bly, S. Ganti, K.B. Whitlock, W.B. Dobyns, J. Perkins, J.T. Bennett, Genotype correlates with clinical severity in PIK3CA-associated lymphatic malformations, JCI Insight 4(21) (2019).

[2] K.C. Kurek, V.L. Luks, U.M. Ayturk, A.I. Alomari, S.J. Fishman, S.A. Spencer, J.B. Mulliken, M.E. Bowen, G.L. Yamamoto, H.P. Kozakewich, M.L. Warman, Somatic mosaic activating mutations in PIK3CA cause CLOVES syndrome, Am J Hum Genet 90(6) (2012) 1108-15.

[3] M. Sadick, R. Muller-Wille, M. Wildgruber, W.A. Wohlgemuth, Vascular Anomalies (Part I): Classification and Diagnostics of Vascular Anomalies, Rofo 190(9) (2018) 825-835.

[4] A. Queisser, E. Seront, L.M. Boon, M. Vikkula, Genetic Basis and Therapies for Vascular Anomalies, Circ Res 129(1) (2021) 155-173.

[5] J.A. Cox, E. Bartlett, E.I. Lee, Vascular malformations: a review, Semin Plast Surg 28(2) (2014) 58-63.

[6] N. Limaye, J. Kangas, A. Mendola, C. Godfraind, M.J. Schlogel, R. Helaers, L. Eklund, L.M. Boon, M. Vikkula, Somatic Activating PIK3CA Mutations Cause Venous Malformation, Am J Hum Genet 97(6) (2015) 914-21.

[7] P. Castel, F.J. Carmona, J. Grego-Bessa, M.F. Berger, A. Viale, K.V. Anderson, S. Bague, M. Scaltriti, C.R. Antonescu, E. Baselga, J. Baselga, Somatic PIK3CA mutations as a driver of sporadic venous malformations, Sci Transl Med 8(332) (2016) 332ra42.

[8] S.D. Castillo, E. Tzouanacou, M. Zaw-Thin, I.M. Berenjeno, V.E. Parker, I. Chivite, M. Mila-Guasch, W. Pearce, I. Solomon, A. Angulo-Urarte, A.M. Figueiredo, R.E. Dewhurst, R.G. Knox, G.R. Clark, C.L. Scudamore, A. Badar, T.L. Kalber, J. Foster, D.J. Stuckey, A.L. David, W.A. Phillips, M.F. Lythgoe, V. Wilson, R.K. Semple, N.J. Sebire, V.A. Kinsler, M. Graupera, B. Vanhaesebroeck, Somatic activating mutations in Pik3ca cause sporadic venous malformations in mice and humans, Sci Transl Med 8(332) (2016) 332ra43.

[9] L. Rodriguez-Laguna, N. Agra, K. Ibanez, G. Oliva-Molina, G. Gordo, N. Khurana, D. Hominick, M. Beato, I. Colmenero, G. Herranz, J.M. Torres Canizalez, R. Rodriguez Pena, E. Vallespin, R. Martin-Arenas, A. Del Pozo, C. Villaverde, A. Bustamante, C. Ayuso, P. Lapunzina, J.C. Lopez-Gutierrez, M.T. Dellinger, V. Martinez-Glez, Somatic activating mutations in PIK3CA cause generalized lymphatic anomaly, J Exp Med 216(2) (2019) 407-418.

[10] T. Hong, X. Xiao, J. Ren, B. Cui, Y. Zong, J. Zou, Z. Kou, N. Jiang, G. Meng, G. Zeng, Y. Shan, H. Wu, Z. Chen, J. Liang, X. Xiao, J. Tang, Y. Wei, M. Ye, L. Sun, G. Li, P. Hu, R. Hui, H. Zhang, Y. Wang, Somatic MAP3K3 and PIK3CA mutations in sporadic cerebral and spinal cord cavernous malformations, Brain 144(9) (2021) 2648-2658.

[11] M. Peyre, D. Miyagishima, F. Bielle, F. Chapon, M. Sierant, Q. Venot, J. Lerond, P. Marijon, S. Abi-Jaoude, T. Le Van, K. Labreche, R. Houlston, M. Faisant, S. Clemenceau, A.L. Boch, A. Nouet, A. Carpentier, J. Boetto, A. Louvi, M. Kalamarides, Somatic PIK3CA Mutations in Sporadic Cerebral Cavernous Malformations, N Engl J Med 385(11) (2021) 996-1004.

[12] A.A. Ren, D.A. Snellings, Y.S. Su, C.C. Hong, M. Castro, A.T. Tang, M.R. Detter, N. Hobson, R. Girard, S. Romanos, R. Lightle, T. Moore, R. Shenkar, C. Benavides, M.M. Beaman, H. Muller-Fielitz, M. Chen, P. Mericko, J. Yang, D.C. Sung, M.T. Lawton, J.M. Ruppert, M. Schwaninger, J. Korbelin, M. Potente, I.A. Awad, D.A. Marchuk, M.L. Kahn, PIK3CA and CCM mutations fuel cavernomas through a cancer-like mechanism, Nature 594(7862) (2021) 271-276.

[13] R. Huo, Y. Yang, Y. Sun, Q. Zhou, S. Zhao, Z. Mo, H. Xu, J. Wang, J. Weng, Y. Jiao, J. Zhang, Q. He, S. Wang, J. Zhao, J. Wang, Y. Cao, Endothelial hyperactivation of mutant MAP3K3 induces cerebral cavernous malformation enhanced by PIK3CA GOF mutation, Angiogenesis 26(2) (2023) 295-312.

[14] K. Banerjee, Y. Lin, J. Gahn, J. Cordero, P. Gupta, I. Mohamed, M. Graupera, G. Dobreva, M.A. Schwartz, R. Ola, SMAD4 maintains the fluid shear stress set point to protect against arterial-venous malformations, J Clin Invest 133(18) (2023).
[15] R. Ola, A. Dubrac, J. Han, F. Zhang, J.S. Fang, B. Larrivee, M. Lee, A.A. Urarte, J.R. Kraehling, G. Genet, K.K. Hirschi, W.C. Sessa, F.V. Canals, M. Graupera, M. Yan, L.H. Young, P.S. Oh, A. Eichmann, PI3 kinase inhibition improves vascular malformations in mouse models of hereditary haemorrhagic telangiectasia, Nat Commun 7 (2016) 13650.
[16] E. Alsina-Sanchis, Y. Garcia-Ibanez, A.M. Figueiredo, C. Riera-Domingo, A. Figueras, X. Matias-Guiu, O. Casanovas, L.M. Botella, M.A. Pujana, A. Riera-Mestre, M. Graupera, F. Vinals, ALK1 Loss Results in Vascular Hyperplasia in Mice and Humans Through PI3K Activation, Arterioscler Thromb Vasc Biol 38(5) (2018) 1216-1229.
[17] D.A. Fruman, H. Chiu, B.D. Hopkins, S. Bagrodia, L.C. Cantley, R.T. Abraham, The PI3K Pathway in Human Disease, Cell 170(4) (2017) 605-635.
[18] A. Angulo-Urarte, P. Casado, S.D. Castillo, P. Kobialka, M.P. Kotini, A.M. Figueiredo, P. Castel, V. Rajeeve, M. Mila-Guasch, J. Millan, C. Wiesner, H. Serra, L. Muixi, O. Casanovas, F. Vinals, M. Affolter, H. Gerhardt, S. Huveneers, H.G. Belting, P.R. Cutillas, M. Graupera, Endothelial cell rearrangements during vascular patterning require PI3-kinase-mediated inhibition of actomyosin contractility, Nat Commun 9(1) (2018) 4826.
[19] W.Y. Aw, C. Cho, H. Wang, A.H. Cooper, E.L. Doherty, D. Rocco, S.A. Huang, S. Kubik, C.P. Whitworth, R. Armstrong, A.J. Hickey, B. Griffith, M.L. Kutys, J. Blatt, W.J. Polacheck, Microphysiological model of PIK3CA-driven vascular malformations reveals a role of dysregulated Rac1 and mTORC1/2 in lesion formation, Sci Adv 9(7) (2023) eade8939.
[20] L. Gambardella, M. Hemberger, B. Hughes, E. Zudaire, S. Andrews, S. Vermeren, PI3K signaling through the dual GTPase-activating protein ARAP3 is essential for developmental angiogenesis, Sci Signal 3(145) (2010) ra76.
[21] S. Dimmeler, B. Assmus, C. Hermann, J. Haendeler, A.M. Zeiher, Fluid shear stress stimulates phosphorylation of Akt in human endothelial cells: involvement in suppression of apoptosis, Circ Res 83(3) (1998) 334-41.
[22] B.G. Coon, N. Baeyens, J. Han, M. Budatha, T.D. Ross, J.S. Fang, S. Yun, J.L. Thomas, M.A. Schwartz, Intramembrane binding of VE-cadherin to VEGFR2 and VEGFR3 assembles the endothelial mechanosensory complex, J Cell Biol 208(7) (2015) 975-86.
[23] E. Tzima, M. Irani-Tehrani, W.B. Kiosses, E. Dejana, D.A. Schultz, B. Engelhardt, G. Cao, H. DeLisser, M.A. Schwartz, A mechanosensory complex that mediates the endothelial cell response to fluid shear stress, Nature 437(7057) (2005) 426-31.
[24] L. Bi, I. Okabe, D.J. Bernard, A. Wynshaw-Boris, R.L. Nussbaum, Proliferative defect and embryonic lethality in mice homozygous for a deletion in the p110alpha subunit of phosphoinositide 3-kinase, J Biol Chem 274(16) (1999) 10963-8.
[25] M. Petkova, M. Kraft, S. Stritt, I. Martinez-Corral, H. Ortsater, M. Vanlandewijck, B. Jakic, E. Baselga, S.D. Castillo, M. Graupera, C. Betsholtz, T. Makinen, Immune-interacting lymphatic endothelial subtype at capillary terminals drives lymphatic malformation, J Exp Med 220(4) (2023).
[26] I. Martinez-Corral, Y. Zhang, M. Petkova, H. Ortsater, S. Sjoberg, S.D. Castillo, P. Brouillard, L. Libbrecht, D. Saur, M. Graupera, K. Alitalo, L. Boon, M. Vikkula, T. Makinen, Blockade of VEGF-C signaling inhibits lymphatic malformations driven by oncogenic PIK3CA mutation, Nat Commun 11(1) (2020) 2869.
[27] S.P. Herbert, J. Huisken, T.N. Kim, M.E. Feldman, B.T. Houseman, R.A. Wang, K.M. Shokat, D.Y. Stainier, Arterial-venous segregation by selective cell sprouting: an alternative mode of blood vessel formation, Science 326(5950) (2009) 294-8.

[28] K. Kunimoto, Y. Yamamoto, M. Jinnin, ISSVA Classification of Vascular Anomalies and Molecular Biology, Int J Mol Sci 23(4) (2022).
[29] T.G. Papaioannou, E.N. Karatzis, M. Vavuranakis, J.P. Lekakis, C. Stefanadis, Assessment of vascular wall shear stress and implications for atherosclerotic disease, Int J Cardiol 113(1) (2006) 12-8.
[30] W.W. Nichols, M.F. O'Rourke, E.R. Edelman, C. Vlachopoulos, McDonald's blood flow in arteries : theoretical, experimental and clinical principles, CRC Press,, Boca Raton, FL, 2022, p. 1 online resource.
[31] W.J. Polacheck, M.L. Kutys, J. Yang, J. Eyckmans, Y. Wu, H. Vasavada, K.K. Hirschi, C.S. Chen, A non-canonical Notch complex regulates adherens junctions and vascular barrier function, Nature 552(7684) (2017) 258-262.
[32] G. Charras, A.S. Yap, Tensile Forces and Mechanotransduction at Cell-Cell Junctions, Curr Biol 28(8) (2018) R445-R457.
[33] C. Bertocchi, Y. Wang, A. Ravasio, Y. Hara, Y. Wu, T. Sailov, M.A. Baird, M.W. Davidson, R. Zaidel-Bar, Y. Toyama, B. Ladoux, R.M. Mege, P. Kanchanawong, Nanoscale architecture of cadherin-based cell adhesions, Nat Cell Biol 19(1) (2017) 28-37.
[34] T.J. Kim, S. Zheng, J. Sun, I. Muhamed, J. Wu, L. Lei, X. Kong, D.E. Leckband, Y. Wang, Dynamic visualization of alpha-catenin reveals rapid, reversible conformation switching between tension states, Curr Biol 25(2) (2015) 218-224.
[35] M. Yao, W. Qiu, R. Liu, A.K. Efremov, P. Cong, R. Seddiki, M. Payre, C.T. Lim, B. Ladoux, R.M. Mege, J. Yan, Force-dependent conformational switch of alpha-catenin controls vinculin binding, Nat Commun 5 (2014) 4525.
[36] D.L. Huang, N.A. Bax, C.D. Buckley, W.I. Weis, A.R. Dunn, Vinculin forms a directionally asymmetric catch bond with F-actin, Science 357(6352) (2017) 703-706.
[37] W.J. Polacheck, M.L. Kutys, J.B. Tefft, C.S. Chen, Microfabricated blood vessels for modeling the vascular transport barrier, Nat Protoc 14(5) (2019) 1425-1454.
[38] H. Wiig, M.A. Swartz, Interstitial fluid and lymph formation and transport: physiological regulation and roles in inflammation and cancer, Physiol Rev 92(3) (2012) 1005-60.
[39] G.H. Lee, S.A. Huang, W.Y. Aw, M.L. Rathod, C. Cho, F.S. Ligler, W.J. Polacheck, Multilayer microfluidic platform for the study of luminal, transmural, and interstitial flow, Biofabrication 14(2) (2022).
[40] D.-H.T. Nguyen, S.C. Stapleton, M.T. Yang, S.S. Cha, C.K. Choi, P.A. Galie, C.S. Chen, Biomimetic model to reconstitute angiogenic sprouting morphogenesis in vitro, Proceedings of the National Academy of Sciences 110(17) (2013) 6712-6717.
[41] V. Vickerman, R.D. Kamm, Mechanism of a flow-gated angiogenesis switch: early signaling events at cell-matrix and cell-cell junctions, Integr Biol (Camb) 4(8) (2012) 863-74.
[42] J.W. Song, L.L. Munn, Fluid forces control endothelial sprouting, Proc Natl Acad Sci U S A 108(37) (2011) 15342-7.
[43] Y. Abe, M. Watanabe, S. Chung, R.D. Kamm, K. Tanishita, R. Sudo, Balance of interstitial flow magnitude and vascular endothelial growth factor concentration modulates three-dimensional microvascular network formation, APL Bioeng 3(3) (2019) 036102.
[44] S. Quintero-Fabian, R. Arreola, E. Becerril-Villanueva, J.C. Torres-Romero, V. Arana-Argaez, J. Lara-Riegos, M.A. Ramirez-Camacho, M.E. Alvarez-Sanchez, Role of Matrix Metalloproteinases in Angiogenesis and Cancer, Front Oncol 9 (2019) 1370.
[45] T. Harada, J. Swift, J. Irianto, J.W. Shin, K.R. Spinler, A. Athirasala, R. Diegmiller, P.C. Dingal, I.L. Ivanovska, D.E. Discher, Nuclear lamin stiffness is a barrier to 3D migration, but softness can limit survival, J Cell Biol 204(5) (2014) 669-82.

[46] C.P. Whitworth, W.Y. Aw, E.L. Doherty, C. Handler, Y. Ambekar, A. Sawhney, G. Scarcelli, W.J. Polacheck, P300 Modulates Endothelial Mechanotransduction of Fluid Shear Stress, Cellular and Molecular Bioengineering 17(5) (2024) 507-523.
[47] P.M. Davidson, G.R. Fedorchak, S. Mondesert-Deveraux, E.S. Bell, P. Isermann, D. Aubry, R. Allena, J. Lammerding, High-throughput microfluidic micropipette aspiration device to probe time-scale dependent nuclear mechanics in intact cells, Lab Chip 19(21) (2019) 3652-3663.
[48] A. Queisser, L.M. Boon, M. Vikkula, Etiology and Genetics of Congenital Vascular Lesions, Otolaryngol Clin North Am 51(1) (2018) 41-53.
[49] C. Aitken, V. Mehta, M.A. Schwartz, E. Tzima, Mechanisms of endothelial flow sensing, Nature Cardiovascular Research 2(6) (2023) 517-529.
[50] Y.S. Li, J.H. Haga, S. Chien, Molecular basis of the effects of shear stress on vascular endothelial cells, J Biomech 38(10) (2005) 1949-71.
[51] M.A. Gimbrone, Jr., J.N. Topper, T. Nagel, K.R. Anderson, G. Garcia-Cardena, Endothelial dysfunction, hemodynamic forces, and atherogenesis, Ann N Y Acad Sci 902 (2000) 230-9; discussion 239-40.
[52] W.J. Polacheck, C.S. Chen, Measuring cell-generated forces: a guide to the available tools, Nat Methods 13(5) (2016) 415-23.
[53] Z. Liu, J.L. Tan, D.M. Cohen, M.T. Yang, N.J. Sniadecki, S.A. Ruiz, C.M. Nelson, C.S. Chen, Mechanical tugging force regulates the size of cell-cell junctions, Proc Natl Acad Sci U S A 107(22) (2010) 9944-9.
[54] P.A. Galie, D.-H.T. Nguyen, C.K. Choi, D.M. Cohen, P.A. Janmey, C.S. Chen, Fluid shear stress threshold regulates angiogenic sprouting, Proceedings of the National Academy of Sciences 111(22) (2014) 7968-7973.
[55] Q. Chen, L. Jiang, C. Li, D. Hu, J.W. Bu, D. Cai, J.L. Du, Haemodynamics-driven developmental pruning of brain vasculature in zebrafish, PLoS Biol 10(8) (2012) e1001374.
[56] T.W. Secomb, J.P. Alberding, R. Hsu, M.W. Dewhirst, A.R. Pries, Angiogenesis: an adaptive dynamic biological patterning problem, PLoS Comput Biol 9(3) (2013) e1002983.
[57] A.R. Pries, T.W. Secomb, Making microvascular networks work: angiogenesis, remodeling, and pruning, Physiology (Bethesda) 29(6) (2014) 446-55.
[58] A.R. Pries, B. Reglin, T.W. Secomb, Structural adaptation of vascular networks: role of the pressure response, Hypertension 38(6) (2001) 1476-9.
[59] K. Abe, M. Takeichi, EPLIN mediates linkage of the cadherin catenin complex to F-actin and stabilizes the circumferential actin belt, Proc Natl Acad Sci U S A 105(1) (2008) 13-9.
[60] D.E. Conway, B.G. Coon, M. Budatha, P.T. Arsenovic, F. Orsenigo, F. Wessel, J. Zhang, Z. Zhuang, E. Dejana, D. Vestweber, M.A. Schwartz, VE-Cadherin Phosphorylation Regulates Endothelial Fluid Shear Stress Responses through the Polarity Protein LGN, Curr Biol 27(14) (2017) 2219-2225 e5.
[61] N. Efimova, T.M. Svitkina, Branched actin networks push against each other at adherens junctions to maintain cell–cell adhesion, Journal of Cell Biology 217(5) (2018) 1827-1845.
[62] K. Wolf, M. Te Lindert, M. Krause, S. Alexander, J. Te Riet, A.L. Willis, R.M. Hoffman, C.G. Figdor, S.J. Weiss, P. Friedl, Physical limits of cell migration: control by ECM space and nuclear deformation and tuning by proteolysis and traction force, J Cell Biol 201(7) (2013) 1069-84.
[63] A.S. Naeem, Y. Zhu, W.L. Di, S. Marmiroli, R.F. O'Shaughnessy, AKT1-mediated Lamin A/C degradation is required for nuclear degradation and normal epidermal terminal differentiation, Cell Death Differ 22(12) (2015) 2123-32.
[64] J. Bertacchini, F. Beretti, V. Cenni, M. Guida, F. Gibellini, L. Mediani, O. Marin, N.M. Maraldi, A. de Pol, G. Lattanzi, L. Cocco, S. Marmiroli, The protein kinase Akt/PKB regulates both prelamin A degradation and Lmna gene expression, FASEB J 27(6) (2013) 2145-55.

[65] Y. Samuels, L.A. Diaz, Jr., O. Schmidt-Kittler, J.M. Cummins, L. Delong, I. Cheong, C. Rago, D.L. Huso, C. Lengauer, K.W. Kinzler, B. Vogelstein, V.E. Velculescu, Mutant PIK3CA promotes cell growth and invasion of human cancer cells, Cancer Cell 7(6) (2005) 561-73.
[66] G.L. Weber, M.O. Parat, Z.A. Binder, G.L. Gallia, G.J. Riggins, Abrogation of PIK3CA or PIK3R1 reduces proliferation, migration, and invasion in glioblastoma multiforme cells, Oncotarget 2(11) (2011) 833-49.
[67] M.M. Salek, P. Sattari, R.J. Martinuzzi, Analysis of fluid flow and wall shear stress patterns inside partially filled agitated culture well plates, Ann Biomed Eng 40(3) (2012) 707-28.
[68] M.L. Rathod, W.Y. Aw, S. Huang, J. Lu, E.L. Doherty, C.P. Whithworth, G. Xi, P. Roy-Chaudhury, W.J. Polacheck, Donor-Derived Engineered Microvessels for Cardiovascular Risk Stratification of Patients with Kidney Failure, Small (2024) e2307901.
[69] A. Boudaoud, A. Burian, D. Borowska-Wykret, M. Uyttewaal, R. Wrzalik, D. Kwiatkowska, O. Hamant, FibrilTool, an ImageJ plug-in to quantify fibrillar structures in raw microscopy images, Nat Protoc 9(2) (2014) 457-63.